Low Aftershock Productivity and Fault Geometry of the 2017 Delaware Earthquake

Karen M. Pearson*[1], Vedran Lekic[1], and Lara Wagner[2]

Abstract

Central and Eastern United States (CEUS) earthquakes are less common than those in the tectonically active West Coast, but their significance is elevated due to higher population densities, less-attenuating bedrock geology, variable site-amplification effects, and a higher proportion of structures prone to damage from shaking. Associating CEUS earthquake focal mechanisms with causative crustal faults is challenging due to a lack of mapped faults. Aftershock productivity of CEUS earthquakes is difficult to predict because it is highly variable, displaying globally typical behavior in some regions (Wu *et al.*, 2015; Wu and Chapman, 2017) and low decay rates (Stein and Liu, 2009; Calais *et al.*, 2016; Toda and Stein, 2018) in others. Here, we study the aftershock sequence of an unusual M_w 4.24 CEUS earthquake that occurred below the Atlantic Coastal Plain east of Dover, Delaware, in late 2017. We analyze data from a temporary 14-station network and use template matching to search for aftershocks, which we locate using a custom 1D velocity model. We find aftershock locations favoring slip on a northwest–southeast-striking fault oblique to the presumed fault where the mainshock was located. We document an unusually low *a* value and large magnitude difference between the mainshock and the largest aftershock, as well as an average aftershock decay *p* value. Factors proposed to explain variations in aftershock productivity include fault alignment relative to the prevailing stress field (Hardebeck, 2010) and low productivity after a high stress drop (Wetzler *et al.*, 2018). We test these hypotheses in relation to the 2017 Delaware earthquake aftershocks, showing the Delaware earthquake had a stress drop of 35 MPa, normal for an intraplate region (Boyd *et al.*, 2017), and had favorable alignment for aftershock thrust faulting. We therefore propose a small fault of possible pre-Mesozoic origin, limiting the productivity observed.

Cite this article as Pearson, K. M., V. Lekic, and L. Wagner (2026). Low Aftershock Productivity and Fault Geometry of the 2017 Delaware Earthquake, *Seismol. Res. Lett.* **XX**, 1–20, doi: 10.1785/0220250322.

Supplemental Material

Background

Introduction

On 30 November 2017, a moment magnitude 4.24 (Kim *et al.*, 2018) earthquake occurred east of Delaware's capital city of Dover. The region has minimal historic seismicity (Stover and Coffman, 1993; Kim *et al.*, 2018) and is in an intraplate location outside of known east coast seismic areas, 80 km from the Lancaster (Pennsylvania) seismic zone, 130 km from the Ramapo fault (New Jersey to New York), and 300 km from the Central Virginia seismic zone (CVSZ) (Fig. 1). This event's epicenter within the Salisbury Embayment of the Atlantic Coastal Plain (ACP) makes it unusual even among east coast earthquakes. As with most of the Central and Eastern United States (CEUS), Delaware and the Salisbury Embayment have no faults recorded in the U.S. Geological Survey (USGS) Quaternary fault database (Data and Resources), and any earthquake that occurs in this region would most likely be due to reactivation of ancient faults.

Other notable earthquakes in Delaware are limited to a modified Mercalli index VII event in 1871 at the Delaware–New Jersey border southeast of Wilmington (Stover and Coffman, 1993) and an M_L 3.8 earthquake in a very similar location southeast of Wilmington in 1973 (Sbar *et al.*, 1975). These are distinct from the 2017 event in that they occurred at the transition from the ACP to the Piedmont (Fig. 1), rather than within the ACP. An earthquake with an estimated magnitude of 3.3 occurred somewhere near Dover in 1879 (Baxter,

1. University of Maryland, College Park, Maryland, U.S.A., https://orcid.org/0000-0002-3548-272X (VL); 2. Carnegie Institution for Science, Washington, D.C., U.S.A.

*Corresponding author: karen.melinda@gmail.com

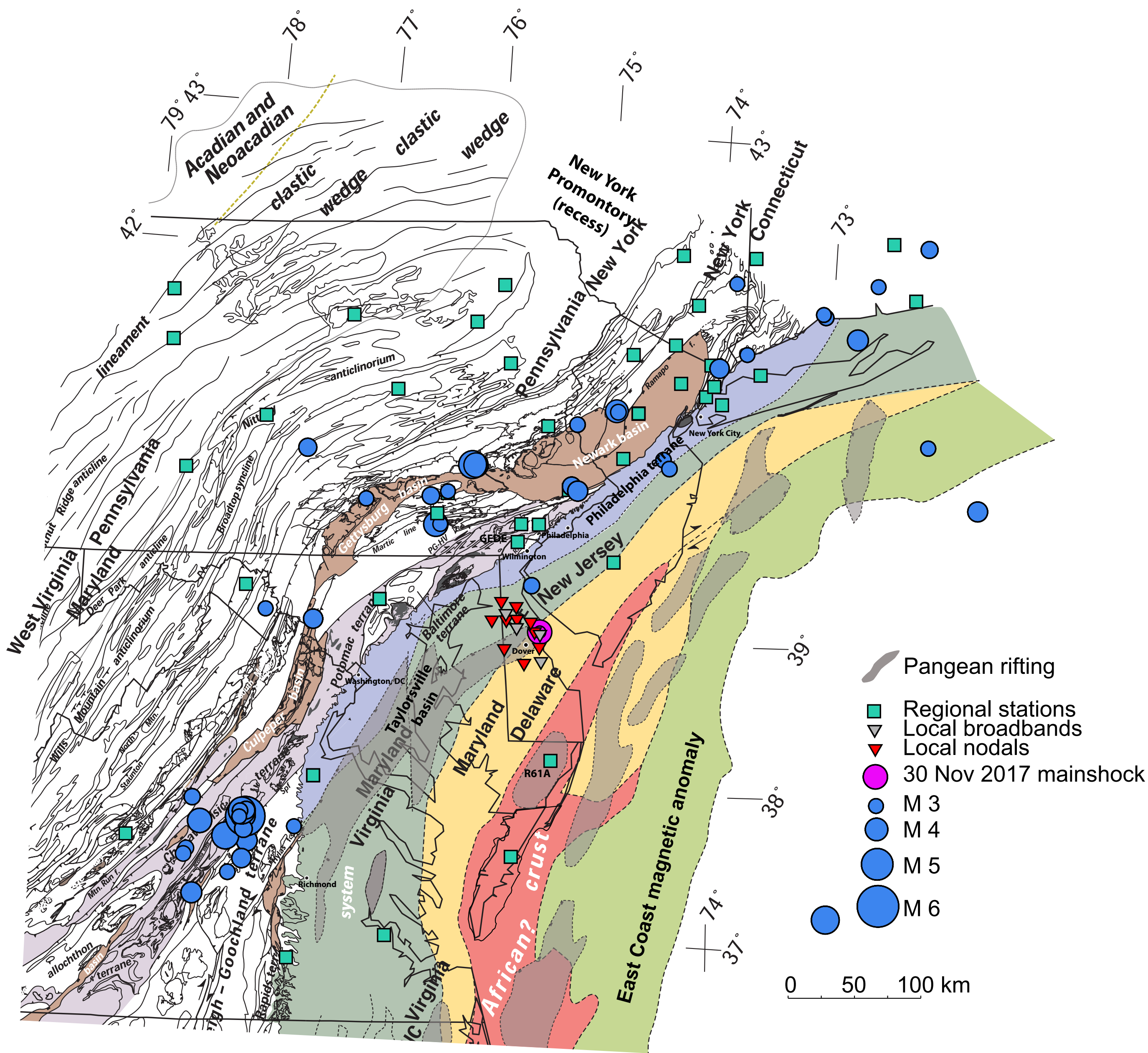

Figure 1. Geologic terrane map of the Mid-Atlantic region of the United States with historic seismicity, regional stations, and local temporary stations. Permanent regional three-component stations at the time of the 2017 Delaware earthquake are shown with green squares. Temporary nodal seismometers are shown with filled red triangles, and temporary broadband seismometers are shown with filled dark gray triangles. The blue circles indicate the locations of all M 3+ earthquakes in the Advanced National Seismic System (ANSS) catalog since 1980, scaled by magnitude (Data and Resources). The epicenter of the 30 November 2017 earthquake is a magenta circle. In Delaware (DE), the green is the Carolina Superterrane, gold is the Brunswick terrane (together these form the Salisbury Embayment), and gray shows the extent of Pangaean rifting. The Culpeper, Gettysburg, and Newark basins shown in light brown are other Triassic–Jurassic basins (Hatcher Jr. *et al.*, 2007; Withjack *et al.*, 2012). Figure modified from Hatcher Jr. *et al.* (2007). The color version of this figure is available only in the electronic edition.

2000; Kim *et al.*, 2018), but primary source information is not accessible to identify an exact source location or felt regions. Beyond Delaware, there have been no other M 4 or greater earthquakes within/under the ACP since 2000 (Advanced National Seismic System [ANSS] Comprehensive catalog, see Data and Resources).

Earthquakes in the CEUS are significant for several reasons. Because of older, colder, and less fractured bedrock geology east of the Rockies, seismic waves can travel much farther while losing less energy than comparable seismic waves in the western U.S. Historic and older, non-retrofitted construction, efficient transmission of seismic waves, and site amplification effects can make even light-to-moderate earthquakes high-risk events within the CEUS. The CEUS has significant aging infrastructure and some of the highest population densities in the country, which could lead to great economic losses and even the potential for human injury if hazards are not properly identified and communicated.

Regional geology and tectonics

East-central Delaware is situated near the northeast end of the estimated extent of the Taylorsville Rift basin, part of the Newark Supergroup of rift basins (Fig. 1; Hatcher Jr. *et al.*, 2007). At the latitude of the Delaware event, this half-graben strikes west-southwest–east-northeast and dips seaward, a result of Triassic rifting (Withjack *et al.*, 1998). The normal faults that formed during the initial rifting of Pangaea shifted to reverse motion during the transition to drifting in the Early Jurassic (Withjack *et al.*, 1998). The southern end of the Taylorsville Rift is exposed in the Piedmont region of central Virginia, and additional extent is inferred from borehole studies, water wells, and geophysical studies (Olsson *et al.*, 1988; LeTourneau, 2003). Seismic surveying in eastern Maryland to the southwest of the mainshock epicenter identified rift basin rocks dipping eastward to the east of the Chesapeake Bay (Hansen, 1988). A graben with a north-northeast strike was also identified about 50 km north of the mainshock location near Delaware City, Delaware (Spoljaric, 1973).

The maximum horizontal stresses in this area strike northeast–southwest (Zoback and Zoback, 1989; Withjack *et al.*, 1998; Heidbach *et al.*, 2018). This is roughly consistent with both the strike of rift structures such as the bounding faults of the Taylorsville basin and the general stress across most of the CEUS, which exhibits a broadly uniform stress field in both magnitude and direction (Zoback and Zoback, 1989; Heidbach *et al.*, 2018). Because the North American plate lacks a subducting edge, the dominant driver of this stress likely comes from ridge push and/or basal drag; Zoback and Zoback (1989) argue that ridge push is the more likely cause of the stress field in the CEUS.

Explanations for seismicity along the east coast of North America have been variably attributed to isostatic rebound from glacial retreat, continental denudation, sediment loading, thermal deformation, plate tectonic sources, crustal thickness variations, and more (see Gardner, 1989, and sources therein; Soto-Cordero *et al.*, 2018). Earthquake locations are often attributed to pre-existing crustal weakness or faults from pre-Quaternary ages (Gardner, 1989).

Previous work

Initial indications in Delaware of a large magnitude difference between the mainshock and the largest aftershock motivated our investigation of parameters governing the detected aftershock sequence. The M_w 4.24 mainshock (Kim *et al.*, 2018) on 30 November 2017 had only one aftershock identified by the USGS (Data and Resources), occurring on 13 December 2017 at 00:45:27 UTC with an estimated local magnitude 1.24 (U.S. Geological Survey [USGS], n.d.a). Preliminary analysis using the regional network and reported in Kim *et al.* (2018) identified one foreshock and eight aftershocks, six of which occurred during this temporary deployment period. The local magnitudes determined by that work for these events ranged from M_L 0.9 to 1.9.

Aftershock sequences are typically described by several statistical "laws," each with one or more characteristic parameters. These parameters are used to quantify the overall productivity, rate of decay, and relative frequency of larger versus smaller magnitude aftershocks. Variations in these parameters can relate to the geologic region being studied, such as the tectonic environment and/or the driving forces of the observed seismicity (i.e., induced earthquakes, volcanic, or geothermal-related).

Ebel (2009) studied a collection of 19 stable continental region (SCR) mainshocks and found the mean magnitude difference between the mainshock and largest aftershock was 1.4 ± 0.7 magnitude units, with a median of 1.3 magnitude units. Those findings were consistent with the difference of 1.2 magnitude units given by Båth's law (Richter, 1958; Båth, 1965).

Factors proposed to explain variations in aftershock productivity include fault alignment relative to the prevailing stress field (Hardebeck, 2010) and low productivity after a high stress drop (Wetzler *et al.*, 2018; Dascher-Cousineau *et al.*, 2020). Productivity for intraplate regions in general has been reported as both lower than the global average (Page *et al.*, 2016) and higher than the global average (Dascher-Cousineau *et al.*, 2020). Dascher-Cousineau *et al.* (2020) observe that productivity is most likely influenced by a combination of stress drop, lithospheric age, and dip (focal mechanism).

Overview of this work

A group of scientists from the University of Maryland, Carnegie Institution for Science, USGS, and others organized a temporary deployment of three-component seismometers installed the day following the mainshock to detect any possible aftershock activity. Here, we report a case study of findings based primarily on data from this temporary deployment, focusing on identifying the fault(s) on which the aftershocks occurred and quantifying the key parameters that characterize the aftershock sequence. We put this sequence into the context of previous observations of aftershock productivity for other earthquakes in SCRs and assess which of the factors above are most likely to apply to this Delaware earthquake.

Data

The nearest permanent seismic station (GEDE/LDSN) is 70 km from the mainshock epicenter and only five stations are within 100 km (Fig. 1). To enable detection of smaller magnitude aftershocks that would not register at those distances, personnel from the Carnegie Institution for Science Department of Terrestrial Magnetism (now Earth and Planets Laboratory), the University of Maryland Department of Geology, and the USGS mobilized the day after the earthquake

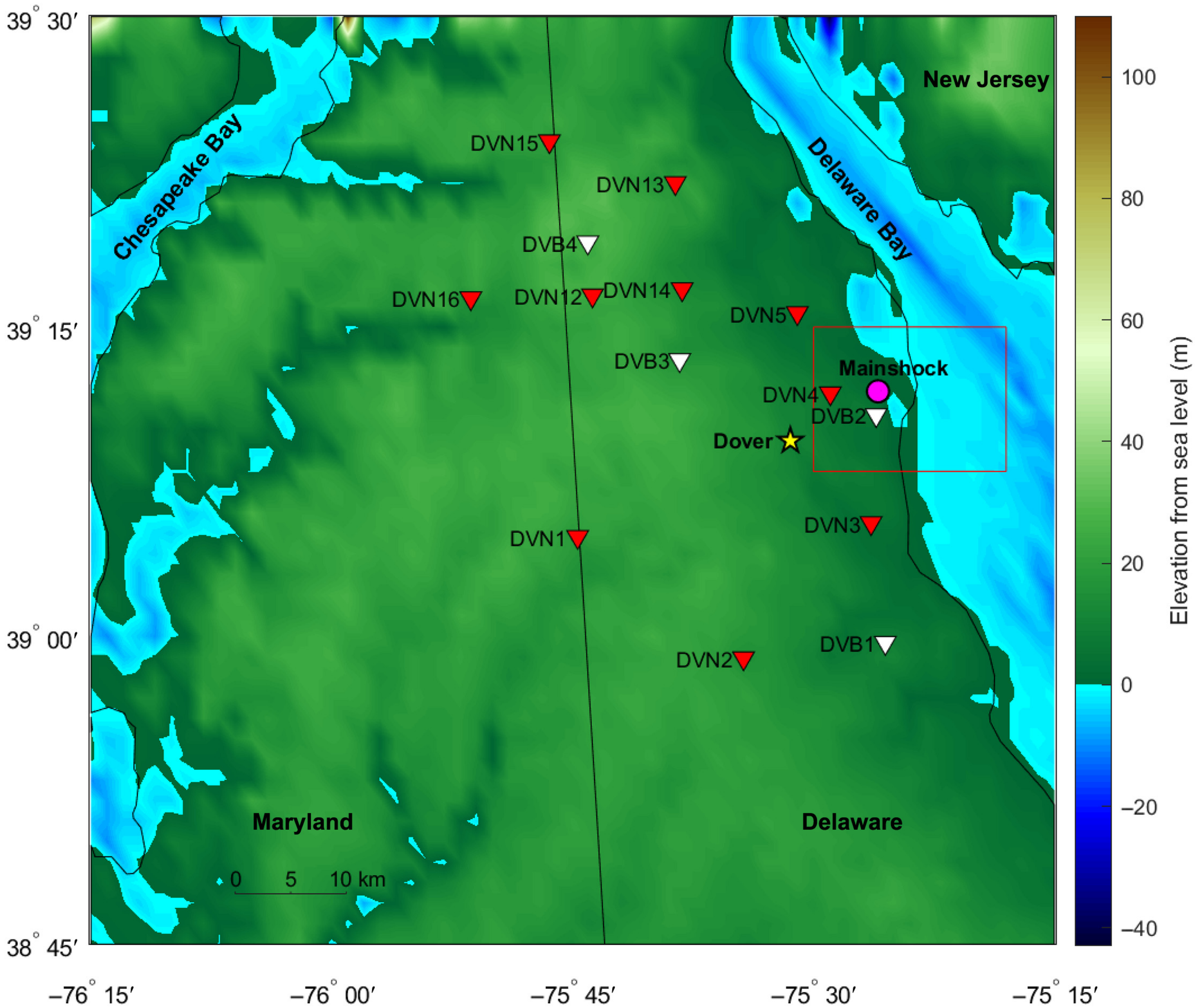

(1 December 2017) to install a temporary local network in the epicentral area using a mix of instruments. A total of 14 instruments were installed in central Delaware and eastern Maryland, covering an area approximately 40 km in diameter. Two broadband and two short-period stations were also deployed by Lamont–Doherty Earth Observatory on the north side of Delaware Bay at distances 20 km and greater from the mainshock (Kim *et al.*, 2018). Because of the distance, these stations did not record aftershocks well and were not included in this study. Stations were deployed over a relatively broad area for a moderate-magnitude mainshock. This allowed for location uncertainty in the mainshock location and for no prior expectations on where aftershocks might be located, without defined faults known. Locations were also governed by the ability to gain landowner permission on short notice. The deployment remained in place until 11 January 2018. The temporary local stations that were deployed on 1 December 2017 are shown in detail in Figure 2.

Figure 2. Local portable seismographic station deployment from 1 December 2017 to 11 January 2018. Stations with broadband sensors are plotted by white triangles and designated "DVB"; short-period sensors (nodals) are plotted by red triangles and designated "DVN". The epicenter of the 30 November 2017 earthquake is a magenta circle. The red box indicates the region where aftershocks were detected, and the borders of the map are shown in Figure 6. Note the coast includes significant tidal wetlands, and so the sea level topography does not exactly align with marked state boundaries (black). The color version of this figure is available only in the electronic edition.

Instrumentation included ten FairfieldNodal ZLand nodes containing three-component 5 Hz geophones provided by the University of Maryland and four Nanometrics Trillium 120 Compact Posthole broadband seismometers provided by the Carnegie Institution for Science. Further details on the deployment are available in Kim *et al.* (2018). Three of the four solar-

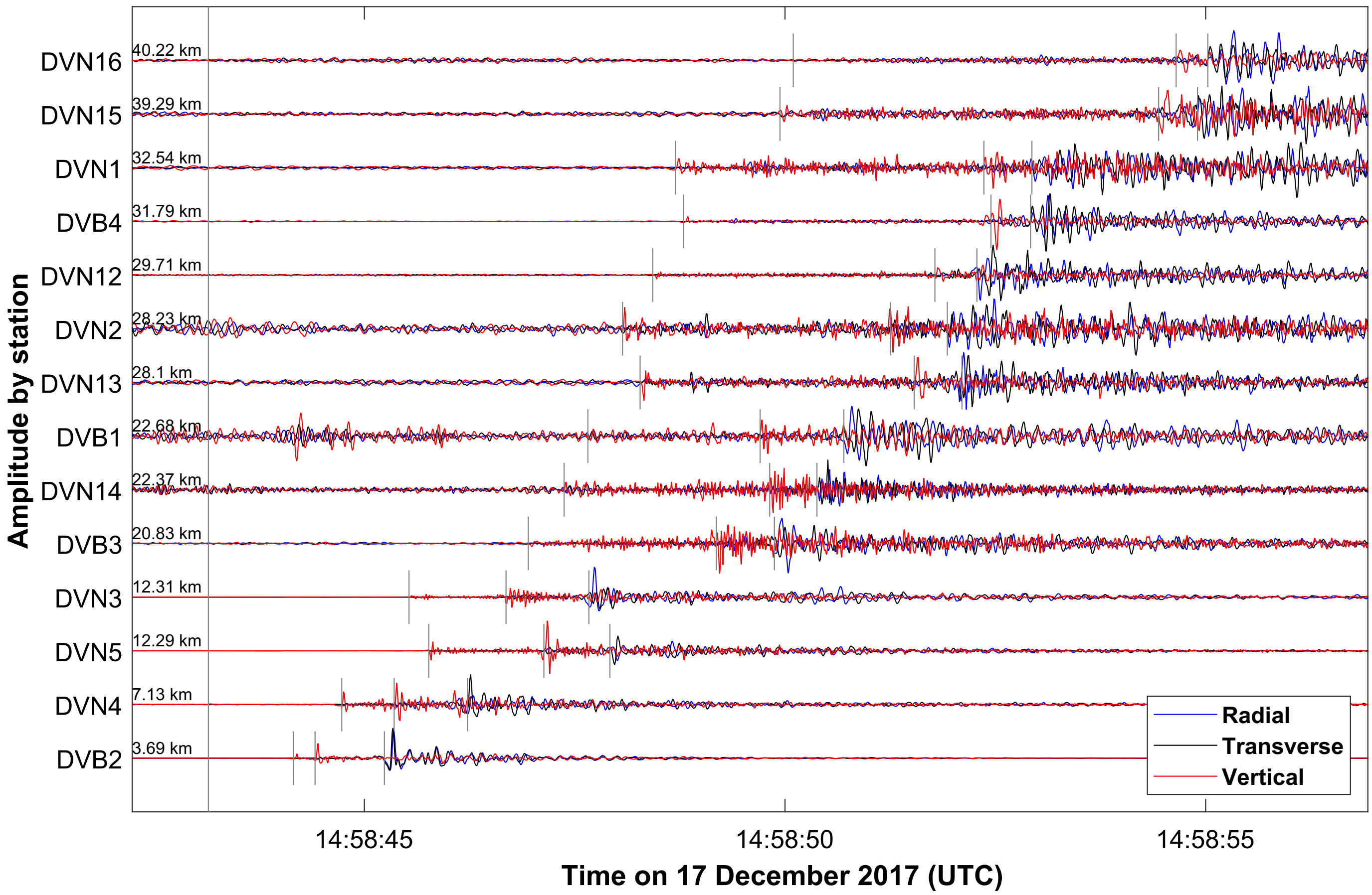

Figure 3. Local station waveforms by distance from the event. Event-to-station distance is given for each station at the start of the trace. The pattern of *Pg*, *SPg*, and *S* arrivals (short gray lines) is exhibited on each station, with the best visibility on the nearer stations. The time between *SPg* and *S* is approximately constant for all distances, and the time between *Pg* and *SPg* lengthens with distance, supporting the interpretation of an *S* wave converting to a *Pg* wave at the sediment layer. The continuous gray line indicates the earthquake origin time. Some marked arrivals are estimated but not used for location determination. Amplitudes for each station are normalized to the maximum recorded for the respective station. The color version of this figure is available only in the electronic edition.

powered compact broadbands, recording 200 samples per second, remained operational until the end of the deployment on 11 January 2018. The ten nodal seismometers, recording 100 samples per second, were battery-operated and remained operational for 37–40 days; locations and end-of-service dates are listed in Table S1, available in the supplemental material to this article.

Methods

Waveform cross-correlation for detection

We used a matched filter waveform correlation technique to identify aftershocks in the data from the temporary deployment (Gibbons and Ringdal, 2006; Schaff and Waldhauser, 2010; Yoon *et al.*, 2015). The largest of the aftershocks detected by Kim *et al.* (2018) was selected as the initial template event. A complete record of the seismograms for the primary template event on 17 December 14:58 at each of the 14 stations is shown in Figure 3.

Using the raw data uncorrected for instrument response, we analyzed the power spectra on each instrument type for a period of 8 s before, during, and after our selected primary template event to ascertain the optimal filtering window and found that the period during the aftershock had elevated power between 4 and 40 Hz relative to nonevent periods for each sensor and component. We therefore used a band-pass filter at 4–40 Hz for raw data from each instrument type. We found the raw waveforms to be more effective at template matching for the high-frequency energy generated by the very small aftershocks we were detecting at close range.

For the initial template, we cut and tapered a waveform segment 12 s long around the *Pg* and *S* arrivals on each data component for each of the 14 deployed stations. The time series for each component (north, east, and vertical) was treated individually in this stage of analysis. Templates were correlated for each of the north, east, and vertical components against all available data for that station, and the algorithm required two components from a given station to be well correlated to their respective templates for that signal to be identified as an aftershock.

Thresholds for each component of data were determined by comparing the distribution of correlation coefficients obtained when correlating the time-reversed template with a day of data, with the distribution of correlation coefficients obtained when correlating the forward, or original, template (Slinkard *et al.*, 2014). In this method, the time-reversed template serves to provide a distribution of correlation coefficients that could be obtained from any random segment of data correlating with that station–component pair. The point at which divergence is observed between the tails of the forward and reverse distributions is considered to be the correlation coefficient threshold for a satisfactory false alarm rate, by removing the false correlations due to noise (which can happen when correlating a waveform in either direction) but retaining the true correlated waveforms of events. Correlation matches are therefore recorded whenever the correlation coefficient exceeds this threshold of divergence from the noise detections. The reader is directed to Slinkard *et al.* (2014) for a more detailed discussion of this approach. We selected a unique correlation threshold for each component and station based on the unique observed noise characteristics. Correlation coefficient thresholds used ranged from 0.4 to 0.6, depending on the station and component, with vertical components accepting lower correlations and the north components requiring the highest correlation to avoid false detections.

In the case of multiple correlation matches recorded for a component within 3 s of each other, the mean time of detection is used as a preliminary event time. To further reduce false alarms, we then compare components for each station with determine when at least two out of three components had detections triggered within 6 s of each other and count these as detections, basing this on the largest measured *S*–*Pg* arrival times for the template event.

Using the first template, we identified 76 potential aftershocks, which were few enough to allow manual inspection of the waveforms for each. Detection capability was significantly better at station DVB2 than any other in the local network, likely due to a high signal-to-noise ratio (SNR) related to a combination of instrument type, low ambient noise at install location, and proximity to aftershocks. DVB2 was located just south of Bombay Hook National Wildlife Refuge, 3.2 km south-southwest of the mainshock epicenter, and about 1.5 km east of Delaware Route 9—a moderately trafficked road that other proximal stations to the epicenter were located much nearer to (Fig. 2). Other stations' positive detections dropped significantly with distance from the mainshock epicenter and very few unique (nonduplicate) detections were added beyond those from DVB2. Both the closest nodal seismometers and the more distant broadbands exhibited high false positive rates, leading us to focus on station DVB2 for further detections with additional templates.

Because the local stations operated in the near field of the aftershocks, small changes in aftershock epicenters result in a comparatively large difference in azimuth, affecting the detected waveform shape (Fig. 4). We selected an additional ten aftershocks to use as templates for additional event detection. For these templates, we elected to only run the correlation detector on data from DVB2 with a reduced template length of 6 s, due to the shorter travel times for this near-field station. Because of diminishing gains in new event detections with each subsequent template, no further templates were used. With these additional ten templates, there were a total of 108 aftershocks detected during the deployment. Over half of the 108 aftershocks were detected only at station DVB2.

Velocity model development

The peninsula between the Chesapeake Bay and Delaware Bay, colloquially known as "Delmarva" due to its makeup of most of the state of Delaware and portions of the states of Maryland and Virginia, is part of the ACP. It extends approximately 270 km north to south and 100 km east to west at its widest point with an elevation of 31 m above sea level.

Previous geophysical work on the ACP is limited and there are no near-surface crustal velocity models specifically developed for central Delaware that would allow for accurate location estimates for the locatable events. Preliminary aftershock identification for the Delaware earthquake done by Kim *et al.* (2018) used the crustal earth model presented by Herrmann (1979), intended for the central United States and including a 1-km surface layer with moderately low velocity. Other models identified for the CEUS and ACP include work done by Dreiling *et al.* (2017), which established *P*- and *S*-wave crustal velocities for the ACP but recognized the need to separately account for surface site conditions.

Studies of the ACP depth to basement vary in methods and results, with no single study providing conclusive answers at the epicentral location. Work by Pratt (2018) developed a model for V_S in the ACP strata from the fundamental frequencies of horizontal spectral ratios, but is derived from arrays located several hundred kilometers south of Delaware and has a depth to basement of 0.6 km. Studies in the Delmarva region using varied sources including seismic profiles and well data found depth to the crystalline, pre-Cretaceous basement is about 2.35 km at Ocean City, Maryland, to the south on the Atlantic Coast (Olsson *et al.*, 1988; Miller *et al.*, 2017). At Island Beach, New Jersey, to the north and on the Atlantic Coast, depth to basement is about 1.1 km (Olsson *et al.*, 1988) and near Lewes, Delaware, about 50 km south of the mainshock epicenter, depth to basement is about 2 km (Olsson *et al.*, 1988). In addition, receiver function modeling by Cunningham and Lekic (2020) at the TA station nearest to the epicenter of the mainshock (R61A) south-southeast of Dover, Delaware, found the thickness of the surface sediment layer is 2 km. More recently, sediment thickness modeling for the ACP based on well logs from Pope *et al.* (2016) show a 1–1.5 km thick sedimentary layer near the mainshock (Boyd

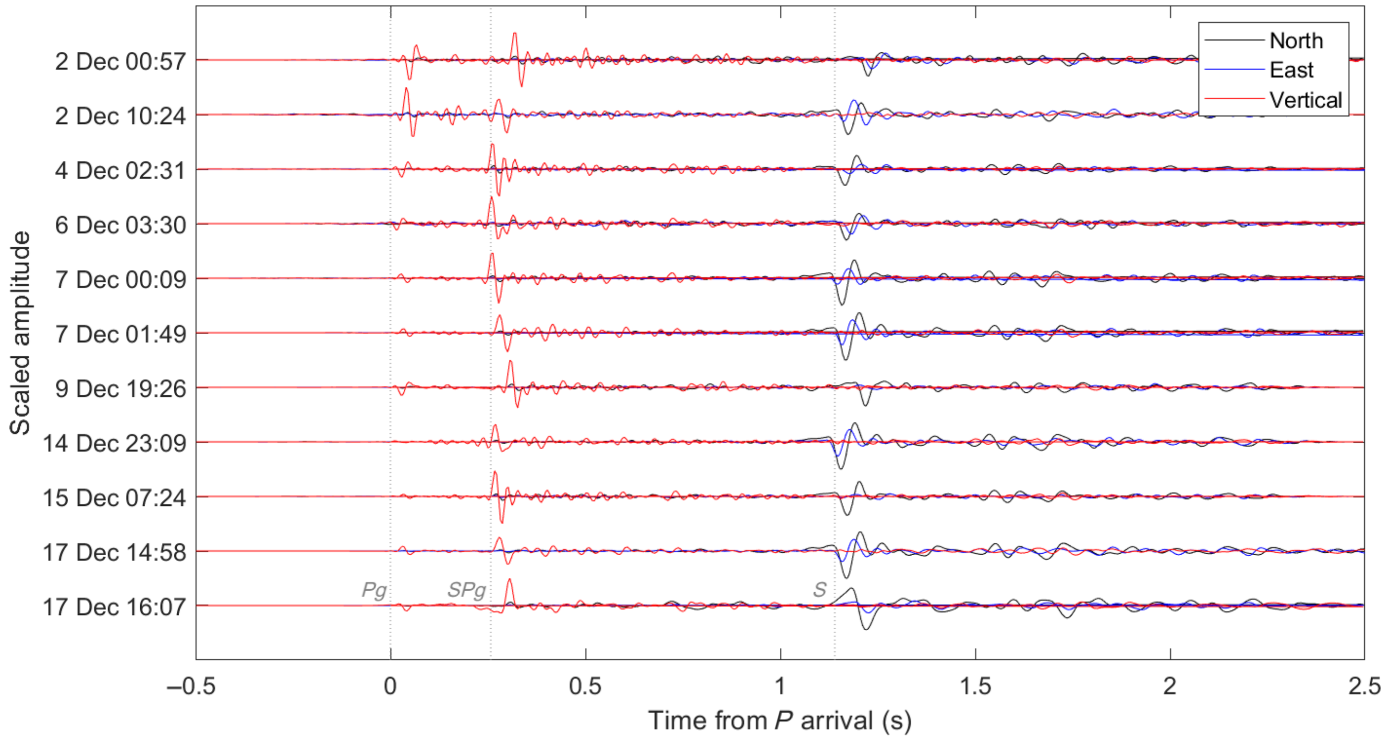

Figure 4. Waveforms for each of the template events at station DVB2 showing north in black, east in blue, and vertical in red. Each event is aligned to have the *Pg* arrival at time 0. The *SPg* converted wave arrival is clear on the vertical component for each of the templates at approximately 0.25 s, marked with a vertical gray line. The *S* wave arrives approximately 1.14 s after the *Pg*, also marked with a vertical gray line. Arrivals are slightly different for each template due to different source locations. Amplitudes for each aftershock are normalized to the maximum recorded for the respective event. The color version of this figure is available only in the electronic edition.

et al., 2024). We chose 2 km as an approximate depth to basement for our location and then determined the appropriate crustal velocities for the upper sediment layers.

We developed a velocity model for use in the location search starting from the model by Dreiling *et al.* (2017). We reduced the top layer of Dreiling *et al.* (2017) ACP model by 2 km corresponding to our surface sediment layer. In the surface sediment layer, the velocities increase rapidly with depth, necessitating thinner layers near the surface and thicker layers deeper down. Therefore, we generate logarithmically spaced points in the sediment pile to define four layers of increasing thickness. Within each layer, the velocities are obtained by computing the harmonic mean of the velocity values within that layer from the continuous velocity profile at the nearest TA station (R61A) from Cunningham and Lekic (2020). Densities for each layer are obtained in the same manner and used solely for model verification. The model was verified by matching waveforms from the M_w 4.24 mainshock observed at the regional station R61A in southern Delaware with synthetic waveforms generated using frequency–wavenumber integration (Saikia, 1994) with the 1D velocity model given in Table 1 (Fig. S1).

TABLE 1
Velocity and Density Model Used for Determining Aftershock Locations and Generating Synthetics Used for Model Verification

Thickness (km)	V_P (km/s)	V_S (km/s)	Density (g/cm^3)
0.030	1.648	0.234	1.7
0.092	2.103	0.549	1.9
0.372	2.611	1.059	2.1
1.506	3.621	1.932	2.3
18	6.0	3.46	2.3
16	6.7	3.87	3.0
∞	8.1	4.68	3.4

The top two kilometers are derived from Cunningham and Lekic (2020) receiver function modeling of crustal sediment at R61A, and the basement layers are from Dreiling *et al.* (2017).

Location search

We manually picked visible *Pg* and *S* arrivals when visible for each of the 108 aftershocks at all temporary local stations. A subset of 39 events was identified as locatable, defined as having at least three stations with waveforms that allowed a seismic analyst to pick body-wave arrival times, with a minimum of three *Pg*-arrival times and one *S*-arrival time. The stations most distant from the mainshock location only detected the largest few aftershocks; some stations recorded low SNR and we could not pick a *Pg* arrival—only an *S* arrival could be picked.

To determine event locations, an iterative grid-search method was used (supplement). The grid center was located southeast of the mainshock by about 3 km just offshore in the Delaware Bay. We used grid spacing of 100 m laterally and 100 m in depth and an overall search region extending 15 km in each direction. Optimal locations for each depth increment were determined based on the minimum residual between the observed travel times and the predicted travel times from each grid location to a station using our crustal velocity model. The residuals for all depth increments were compared and the depth with the least residual was determined to be the optimal depth, with the grid location for that depth as the optimal epicenter.

Source parameters

For all events large enough to locate, we determined a local magnitude using the relation for M_L calibrated for eastern North America (ENA) intraplate events (Kim, 1998):

$$M_L = \log_{10} A + 1.55 \log_{10} X - 0.22 + C, \quad (1)$$

in which C is a station correction term and X is the epicentral station-to-event distance in kilometers. The amplitude A is determined by removing instrument response and convolving the signal with the Wood–Anderson seismograph response, then measuring the maximum horizontal-component body-wave amplitude (in mm). The station correction, given in the Table S1, is calculated from the mean of the station residuals following the method given in Kim (1998).

Using these magnitudes, we obtained the Gutenberg–Richter relation between magnitude and number of events detected while the local network was deployed, $\log_{10} N(\geq m) = A - bm$. We performed an iterative search for the linear portion of the fit to the log-cumulative frequency-magnitude counts adjusting both the lower (M_c) and upper limits of the magnitude range in 0.1 magnitude increments. We selected the magnitude range which minimized the error of the least-squares fit, so that fitting is only done within the magnitude range in which the observed frequency-magnitude relationship is close to linear.

To test the hypothesis of high stress drop causing the low productivity observed for the Delaware aftershock sequence, we determined the stress parameter estimate for the M_w 4.24 mainshock using the Brune model (Brune, 1970) for a circular rupture. The choice of constant k in this model can lead to stress parameter estimates differing by more than a factor of five (Brune, 1970; Madariaga, 1976; Kaneko and Shearer, 2014). We use the value for k derived by Kaneko and Shearer (2014), which models a dynamic rupture with no singularities and results in stress parameter estimates between those of Brune and Madariaga. We fit the model to the *P*-wave and *S*-wave spectra for the mainshock and our primary template aftershock at regional stations, computed the corner frequency for the mainshock model fit by modeling the best-fit power spectral ratio between the mainshock and largest aftershock, and used the resulting value to calculate the stress parameter and rupture radius (supplement).

Aftershock productivity analyses

We used a Bayesian Markov Chain Monte Carlo (MCMC) simulation (supplement) to further constrain the parameters a and b noted above, but now also including c and p as described in the Omori decay rate equation:

$$\lambda(t, M_{\min}) = 10^{a+b(M_{\text{main}}-M_{\min})}(t+c)^{-p}, \quad (2)$$

(Omori, 1895; Utsu, 1961; Reasenberg and Jones, 1989). We use the ensemble model of solutions to quantify the posterior likelihood for each parameter, and their tradeoffs with one another.

Results

Near-surface phase conversion

We observed a strong secondary arrival on the vertical component before horizontal arrivals, which we interpreted to be an *S*-to-*Pg* (*SPg*) wave arriving due to conversion at the raypath transition for the sediment layer occurring in the ACP (Fig. 3). A wave conversion at the sediment layer has previously been reported in the Mississippi Embayment by Chen *et al.* (1996). Daniels *et al.* (2019) observed wave conversion in South Carolina, where the upgoing S-wave converted to a horizontally propagating *P* wave. However, we do not interpret the ray path as horizontally propagating in our case because our *SPg* arrival is strongest on the vertical component rather than the radial throughout the array (Figs. 3 and 4). Furthermore, the time between arrival of the *SPg* and *S* phases is more consistent than that of *Pg* and *SPg*, suggesting the upgoing ray travels as an *S* wave until it converts and traverses the shallow sediment layer vertically as a *P* wave (Fig. 3). The thinning of the sediment layer of the ACP moving westward from the coast appears in the closer spacing between the observations for the *SPg* and *S* phase arrivals (Fig. 5; see Fig. 2 for station location reference), further supporting our hypothesis that this arrival is an *SPg* phase.

Aftershock locations

A total of 39 out of the 108 detected aftershocks had sufficient phase picks to allow event location. Aftershocks are located primarily just offshore and below the Delaware Bay, with depths ranging from 0.5 to 6.5 km (Table 2, Fig. 6). There did not appear to be any temporal progression in aftershock locations. The northeast group of aftershocks are almost exclusively 2.1 km in depth, just below the sediment layer. The

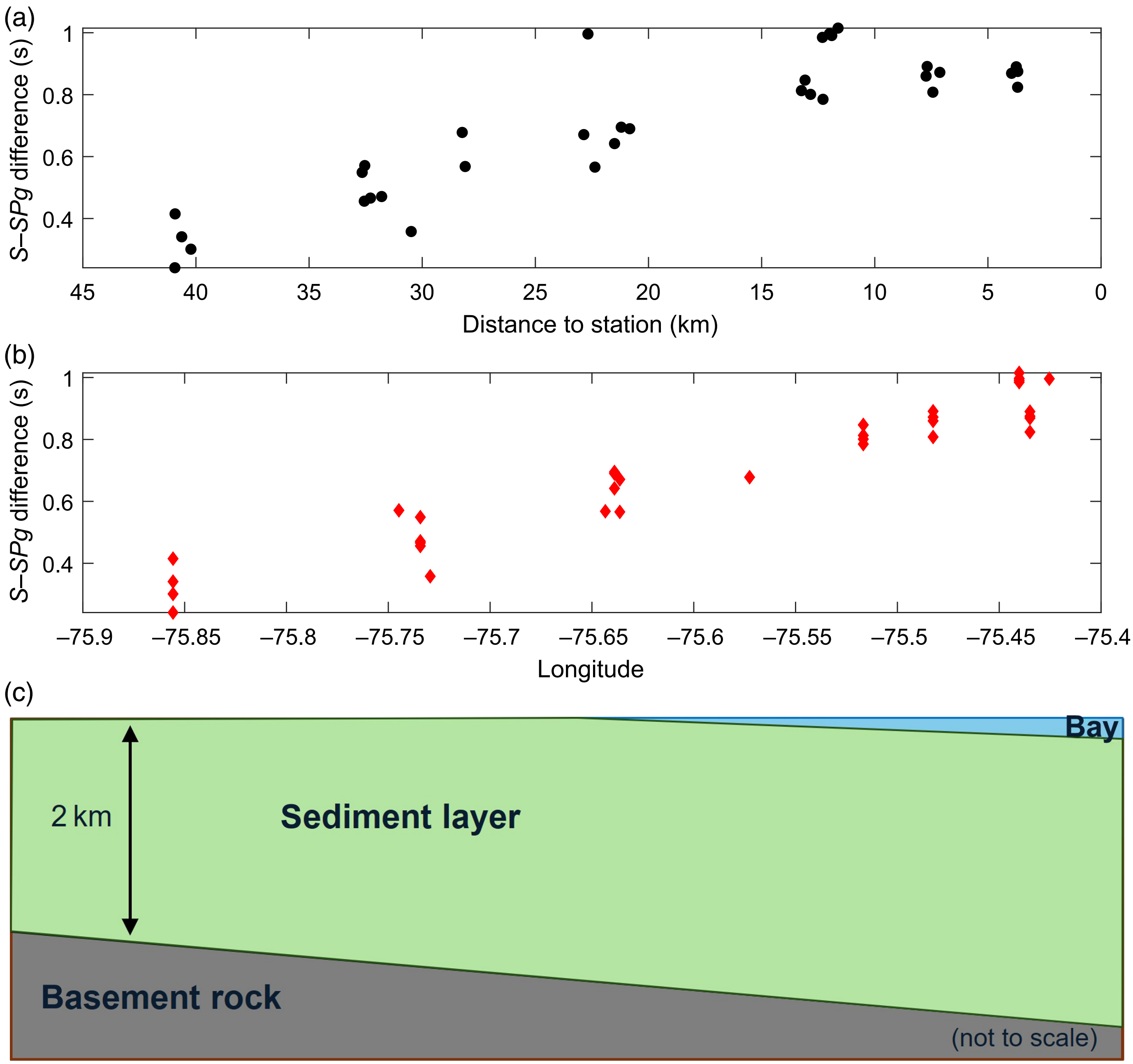

majority of aftershocks fall on a plane striking northwest–southeast and dipping to the southwest (Fig. 5). The southwestern shallow aftershocks with depths from 0.5 to 2 km appear to originate in the sediment. We find aftershock epicenters somewhat farther to the east as well as a slightly different strike than Kim *et al.* (2018). Similarly, the mainshock may have been located a few kilometers farther east, had it been located with this network. These discrepancies may be due to the addition of more local seismic data in our analyses.

The one-sigma error contours for all located aftershocks are shown in Figure S2 in the supplemental material, and the maximum $1 - \sigma$ radial errors are listed in Table 2. Depth uncertainty is constrained to the aftershock location in either the sediment layer or basement rock (Table 2, Fig. S3) and thus is variable in the shallower and deeper sections. Our evaluations of uncertainty are limited to the depths included in the grid search (0.5–8.0 km). Figure 6 shows the one-sigma

Figure 5. Difference in phase arrival time *S–SPg* relative to event-to-station distance (a) and to longitude (b). There is a stronger correlation between *S–SPg* time and longitude (b) than between *S–SPg* and distance (a), corresponding to the thickening of the sediment layer moving toward the coast (eastward). Note in (a) the reversed axis because events are located near the coast or beneath the Delaware Bay, and thus distance increases both westward and north/southward. Notional diagram of the thickening sediment wedge is depicted in (c). The color version of this figure is available only in the electronic edition.

TABLE 2

Dates, Times (UTC), Epicentral Locations, Depths, Local Magnitudes, Horizontal Location 1–σ Error, and 90% Confidence Bounds for Depth of 39 Located Aftershock Events

Date (yyyy/mm/dd) Time (hh:mm:ss.s)	Latitude	Longitude	Depth (km)	M_L	σ Error (km)	90% Depth Confidence (km)
2017/12/01 21:41:33.6	39.218	–75.362	2.1	–0.60	0.35	2.1–4.3
2017/12/01 23:27:32.1	39.201	–75.368	2.1	–0.07	0.55	2.1–4.9
2017/12/02 00:57:40.1	39.165	–75.476	2.0	–0.24	0.44	0.5–2.0
2017/12/02 10:24:44.6	39.197	–75.352	2.1	0.07	0.81	2.1–5.8
2017/12/02 14:36:14.6	39.199	–75.367	2.1	0.39	1.15	2.1–6.9
2017/12/02 18:38:43.1	39.211	–75.365	2.1	0.95	0.68	2.1–5.3
2017/12/04 02:31:26.2	39.236	–75.368	2.1	0.41	0.92	2.1–7.3
2017/12/04 12:13:39.5	39.193	–75.370	2.1	0.81	1.06	2.1–6.9
2017/12/05 01:23:59.3	39.206	–75.364	2.1	0.20	1.16	2.1–6.3
2017/12/06 03:30:09.0	39.166	–75.389	0.5	–0.73	0.07	0.5–1.2
2017/12/07 00:09:27.2	39.159	–75.373	5.7	–0.97	0.07	5.65–5.75
2017/12/07 00:44:01.6	39.203	–75.372	2.1	0.20	0.90	2.1–6.0
2017/12/07 01:49:06.0	39.151	–75.391	6.5	0.69	0.19	6.4–6.6
2017/12/07 18:53:52.7	39.187	–75.358	2.1	0.33	0.94	2.1–6.3
2017/12/07 19:39:39.2	39.211	–75.364	2.1	1.01	1.08	2.1–6.9
2017/12/08 12:17:48.4	39.202	–75.352	2.1	0.82	1.13	2.1–7.1
2017/12/08 14:19:49.3	39.172	–75.486	0.5	0.42	0.45	0.5–2.0
2017/12/09 19:26:58.6	39.204	–75.357	2.1	1.01	0.98	2.1–6.7
2017/12/09 20:26:18.2	39.161	–75.392	1.4	–0.19	0.11	0.5–2.0
2017/12/11 22:02:39.9	39.193	–75.397	6.4	1.29	1.31	3.7–8.0
2017/12/12 04:24:57.5	39.145	–75.454	0.6	–0.16	0.07	0.5–1.3
2017/12/13 00:45:24.4	39.193	–75.393	6.4	1.62	1.19	3.5–8.0
2017/12/14 17:50:51.3	39.168	–75.392	2.0	–0.02	0.07	1.7–2.0
2017/12/14 23:09:51.0	39.171	–75.426	5.2	–0.81	1.20	2.1–8.0
2017/12/15 07:24:09.7	39.197	–75.358	2.1	0.34	0.78	2.1–5.5
2017/12/17 14:58:43.3	39.198	–75.400	5.9	1.75	1.06	2.1–8.0
2017/12/17 16:07:04.7	39.190	–75.394	6.0	1.31	1.40	3.0–8.0
2017/12/19 10:34:59.3	39.207	–75.360	2.1	0.14	0.79	2.1–5.9
2017/12/23 00:57:46.0	39.200	–75.345	2.1	–0.01	1.03	2.1–6.9
2017/12/23 13:29:50.9	39.186	–75.397	4.8	0.56	1.41	2.9–6.6
2017/12/23 16:21:51.6	39.207	–75.387	2.5	0.25	0.90	2.1–6.2
2017/12/27 14:11:44.7	39.211	–75.370	2.1	0.59	0.86	2.1–6.0
2017/12/27 14:32:23.1	39.169	–75.484	0.5	0.29	0.15	0.5–2.0
2017/12/28 05:39:22.7	39.186	–75.367	2.6	–0.40	0.63	2.1–5.2
2017/12/28 09:42:24.9	39.209	–75.367	2.1	–0.12	0.87	2.1–6.0

(Continued next page.)

TABLE 2 (continued)

Dates, Times (UTC), Epicentral Locations, Depths, Local Magnitudes, Horizontal Location 1−σ Error, and 90% Confidence Bounds for Depth of 39 Located Aftershock Events

Date (yyyy/mm/dd) Time (hh:mm:ss.s)	Latitude	Longitude	Depth (km)	M_L	σ Error (km)	90% Depth Confidence (km)
2017/12/30 12:48:56.7	39.193	−75.397	0.5	−0.66	0.07	0.5–2.0
2017/12/31 00:11:18.9	39.203	−75.358	2.1	0.72	1.13	2.1–7.2
2018/01/01 22:37:39.2	39.204	−75.377	4.6	0.51	1.07	2.1–7.5
2018/01/02 05:36:19.3	39.207	−75.367	2.1	0.43	0.72	2.1–5.7

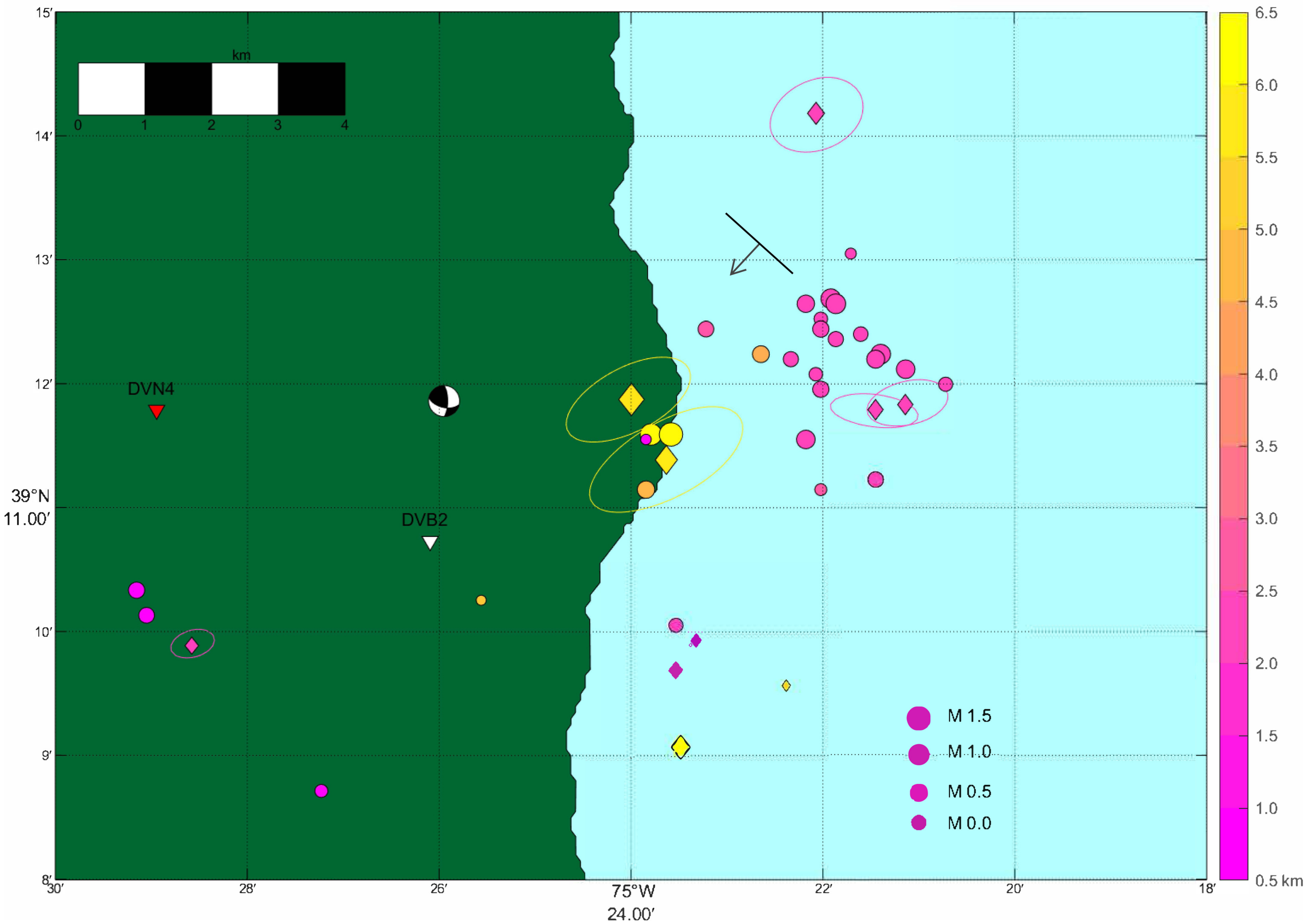

Figure 6. Locations of aftershocks. Shading corresponds to the depth of the event. The size of the marker is proportional to the event's local magnitude; see key for scale. Diamond-shaped markers indicate the events used as templates for aftershock detection and are shown with their one-sigma horizontal error contour. The mainshock location and moment tensor are from Kim *et al.* (2018) and had an approximate depth of 3 km and horizontal location error of ±2.5 km. Only the two nearest stations of the local deployment are visible in this projection; see Figure 2 for the context of location in Delaware. The color version of this figure is available only in the electronic edition.

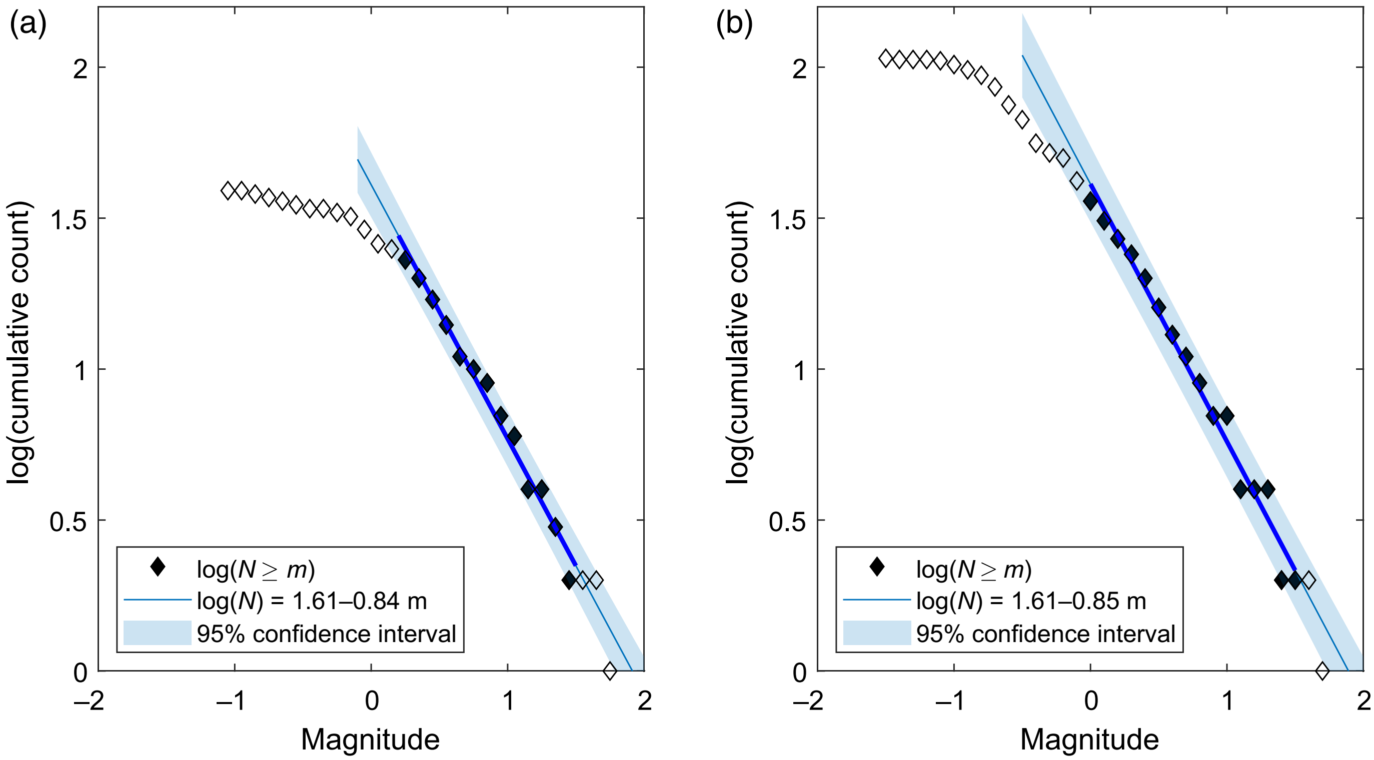

Figure 7. Gutenberg–Richter relation showing relative frequency versus magnitude of located aftershocks during the deployment period of the local network (a). Local magnitudes are calculated using Kim (1998) formula for eastern North America (ENA). Filled counts are those used for determining the best-fit linear regression. The light blue shading shows the 95% confidence of the fit regression. (b) As in (a), but for all 108 detected aftershocks using magnitudes determined from extrapolated distance for those without location. The color version of this figure is available only in the electronic edition.

error contours for the aftershocks used as templates as a representative example of errors for location accuracy. However, we also observed that for the small-magnitude template aftershocks, the location error was at times smaller than the pictured marker. Although additional data are generally known to reduce error, the overdetermined solution for 3D source location plus source time resulted in smaller errors present for the aftershocks, with fewer picks used to resolve the location. Although the χ-square function used to determine the one-sigma error accounts for the number of data going into it (in this case, the number of valid *P* or *S* picks), we find there is additional unmodeled error that grows with additional data used from the more distant stations. The larger aftershocks using more arrival times from more distant stations are more sensitive to errors due to using a 1D crustal velocity model for the 3D sediment wedge of the ACP (Fig. 5), as well as having greater sensitivity to human error in arrival-time picking with lower SNRs.

Locations are generally consistent when the velocity model is adjusted to use a 1-km sediment layer (Fig. S4, Table S2). The distribution follows the same pattern, indicating a northwest–southeast-, southwest-dipping fault plane for aftershocks, but epicenters are up to 1 km farther east and south under the Delaware Bay. The shallower events have depths near the new sediment–basement transition (1.1–1.7 km instead of 2.1–2.6 km), and the deeper events shift to hypocenters about 0.2 km deeper on average. The changes in epicenters result in absolute changes in local magnitude averaging 0.2 units, though the distribution of positive and negative changes is sufficiently even such that the average change is near 0.

Aftershock magnitudes

Local magnitudes for the 39 located aftershocks are given in Table 2. Our aftershock magnitude estimates are consistent with those found by Kim *et al.* (2018). The largest magnitude aftershock was M_L 1.75, resulting in the difference between the mainshock and largest aftershock $\Delta m = 2.45$, more than twice the typical difference $\Delta m = 1.2$ given by Båth's law (Richter, 1958; Båth, 1965).

The detection magnitude of completeness is approximately $M_c = 0.2$ (Fig. 7a), and the *b* value of the best-fit least-squares model for $0.2 \le M \le 1.5$ is 0.84, with a corresponding *A* value of −1.61. Using the Aki (1965) method of estimating the *b* value for the 39 earthquakes located, we obtain a value of 0.83, with a standard error of 0.14 determined using the method of Shi and Bolt (1982).

We extrapolated magnitudes for the remaining 69 detected aftershocks as described in the supplemental material using the relationship between *S–Pg* arrival time versus event-to-station distance for located events (Fig. S5). We were able to use the total catalog of 108 aftershocks and lower our magnitude of completeness to $M_c = 0$. We again applied Aki (1965) method for b value estimation and plotted the Gutenberg–Richter relation (Fig. 7b) to compare it with the smaller sample size above. In this case, the estimate using the Aki (1965) method was $b = 0.86$, with standard error (Shi and Bolt, 1982) equal to 0.11, which overlaps substantially with the estimate for 39 events and is very close to the least-squares estimate of $b = 0.85$ for 108 events, with $A = -1.61$.

Stress-drop estimation

We fit the power spectral ratio model (supplement) to the P-wave and S-wave spectra for the mainshock and our primary template aftershock at several nearby regional stations (see Fig. 1 for locations; see Data and Resources). A table of the best-fit corner frequencies by station and body-wave type is provided in Table S3. An example of the mainshock and aftershock spectra and spectral ratio modeling for the station GEDE is shown in Figure 8.

We determine the mean stress drop was 41 MPa with one standard deviation of ±35 MPa, and the median stress drop is 35 MPa, and the median rupture radius is 323 m. Because of the difficulty in measuring the corner frequency at different stations, our estimates have a high uncertainty level, making it difficult to draw firm conclusions about our stress drop (Abercrombie and Baltay, 2025). In addition, values for k in the circular rupture model are not always reported, contributing to the difficulty in making meaningful comparisons with other studies. For completeness, we note that the estimated stress drop appears typical for an intraplate earthquake in the ENA (Boyd *et al.*, 2017). In comparison, the 2011 M_w 5.7 Mineral, Virginia, earthquake stress drop was variably reported as unusually high (50–75 MPa) (Ellsworth *et al.*, 2011; Wu and Chapman, 2017), even by ENA standards, and as a more usual ENA value of 15–25 MPa (Hartzell *et al.*, 2013) or 17–39 MPa (Boyd *et al.*, 2017). The 2024 M_w 4.8 Tewksbury, New Jersey, earthquake had a stress drop of 2.3–18 MPa and 13–104 MPa for the Brune and Madariaga models, respectively (Beaucé *et al.*, 2025).

A study of global seismicity shows intraplate earthquakes have stress drops about two times higher than for interplate events (Allmann and Shearer, 2009), and a study of North American seismicity found stress drops in ENA around three times higher than central and western North America on average (Boyd *et al.*, 2017). Considering the stress drop of 35 MPa is within the typical range, we therefore do not attribute stress drop as the cause for the low aftershock productivity in Delaware and do not examine this further.

Aftershock productivity parameters

Our MCMC inversions determined optimal values for a, b, c, and p, as shown in Figure 9. For all four parameters, our ensemble mean and median were within 3% of each other. Because we are interested in quantifying the uncertainty of the specific aftershock parameters on their own without making assumptions about preferred values of other model variables, the distributions shown in Figure 9 integrate out all the other parameters to obtain the marginal probability that accounts for uncertainty arising from the tradeoffs with the estimates of the other parameters (Fig. S6). The estimates are compared in Table 3 to values from Page *et al.* (2016) and Ebel (2009).

Discussion

Productivity

The 30 November 2017 M_w 4.24 Delaware mainshock was followed by a maximum M_L 1.75 aftershock on 17 December 2017 (Table 2), giving $\Delta m = 2.45$, much higher than Båth's law's nominal value of 1.2 (Richter, 1958; Båth, 1965). Båth's law indicates that the largest aftershock generally has about 50 times less energy than the mainshock, given a 1.2 magnitude unit difference. In the case of the 2017 Delaware earthquake, the largest aftershock was an additional 1.25 magnitude units lower than expected, indicating it had 125 times less energy than expected and 10,000–15,000 times less energy produced than the mainshock.

To compare the magnitudes on a more equal basis, we convert the mainshock's moment magnitude to the local magnitude scale. Using the scaling for $4.3 < m_b(Lg) < 6.0$ in Rigsby *et al.* (2014) for M_w 4.24, this gives an $m_b(Lg)$ of 4.7. This is in line with the published value of 4.6 in ComCat (Data and Resources). In Kim (1998), he provides the relation between his local magnitude and $m_b(Lg)$, which results in M_L 4.54. Using this to compare with the Delaware earthquake's M_L 1.75 largest aftershock, we find the mainshock–aftershock difference to be $\Delta m = 2.79$ (Table 4), an even larger value than the uncorrected $\Delta m = 2.45$, and an even greater difference from the expected $\Delta m = 1.2$ (Richter, 1958; Båth, 1965). Using Kim (1998) to convert the largest aftershock magnitude to $m_b(Lg)$, we find a difference of $\Delta m = 2.95$.

Båth's law is based on measurements of earthquake magnitudes using the surface-wave magnitude, M_s. The M_s magnitude scale is not suitable for small, local events (Chung and Bernreuter, 1981). An empirical relationship between m_b and M_s is challenging to define, given the inherently different wave types and frequencies used for each (Chung and Bernreuter, 1981). Chung and Bernreuter (1981) provide a regression between m_b and M_s for western U.S. data with an m_b correction for eastern U.S. data, but this is used for magnitudes 4.5 and greater. Lienkaemper (1984) also has a conversion from m_b to M_s, yet it is intended for magnitudes 7 and greater. The values we calculated for $m_b(Lg)$ can be taken as equivalent to m_b magnitudes (Nuttli, 1973; Chung and Bernreuter, 1981), and we use this with the Lienkaemper (1984) formula to estimate M_s for the Delaware mainshock and aftershock.

Table 4 shows the magnitude differences between the mainshock and aftershock using M_L, $m_b(Lg)$, M_s, and M_w for comparison. The M_s difference is very large, but the formula used

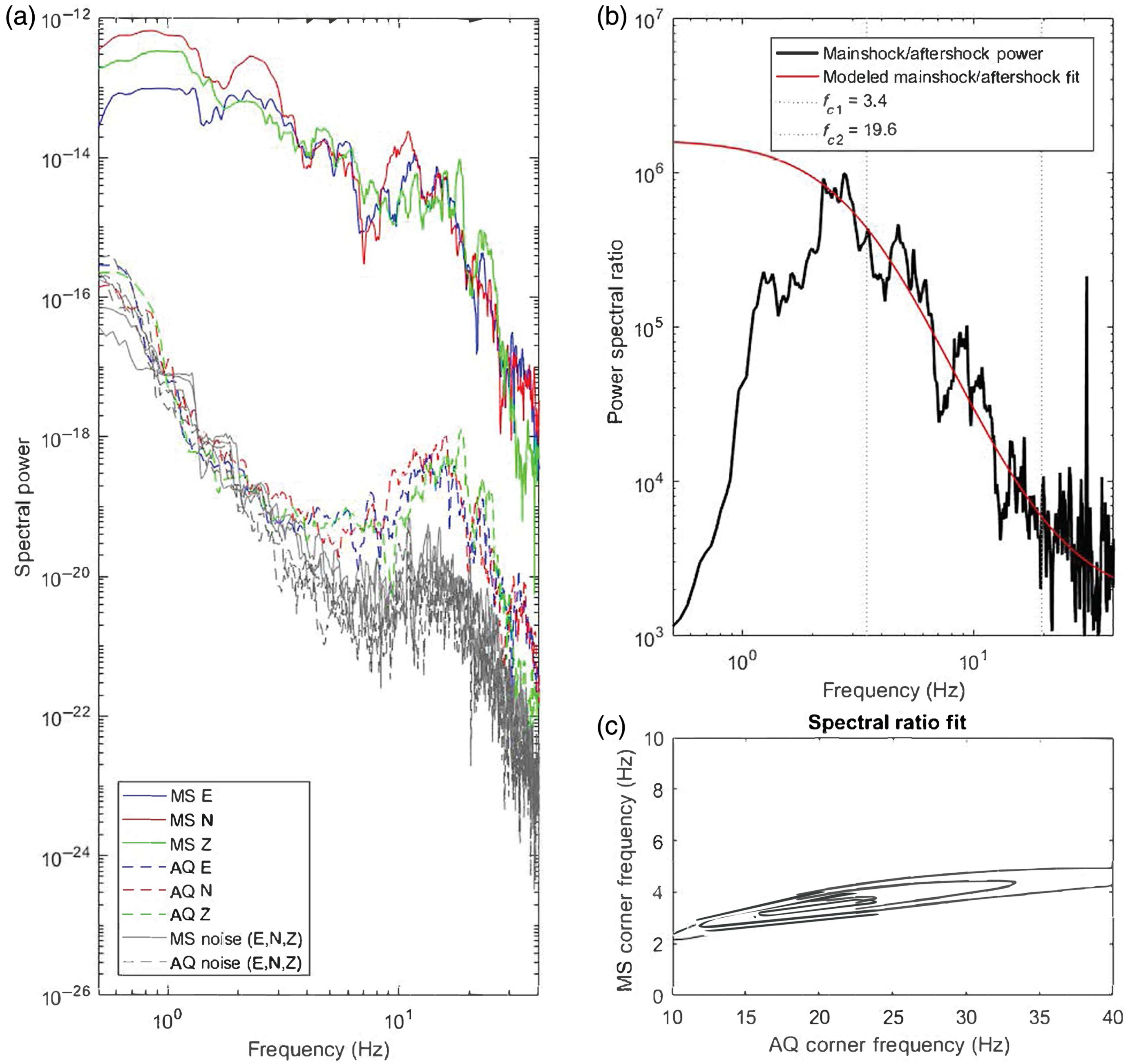

in that case may not be applicable. The M_w difference is smaller, though still above the nominal 1.2-unit difference for Båth's law. Taken together, the range of possibilities for Δm using different calculated magnitudes for this event's mainshock and aftershock indicates that the difference $\Delta m = 2.45$ is likely not a bad estimate for the true value of the difference.

Page *et al.* (2016) presented SCR parameters for five aftershock sequences that followed M ≥ 6.4 mainshocks between 1990 and 2015. Ebel (2009) investigates SCR aftershock parameters for 13 aftershock sequences following M ≥ 5 mainshocks between 1968 and 2008. Both Page *et al.* (2016) and Ebel (2009) used the Reasenberg and Jones (1989) formulation for Omori decay, consistent with this study, but their methods for calculating the parameters vary. They both also include global

Figure 8. (a) Mainshock ("MS") *P*-wave spectral power (solid lines) and M_L 1.75 aftershock ("AQ") on 17 December 14:58 (dashed lines) at station GEDE. For both events, blue is east, red is north, and green is vertical-component data. Noise windows before each event are gray. (b) The mainshock spectral power to aftershock spectral power ratio is shown in solid black. The best-fit spectral ratio model using these two events is shown in red. Thin gray lines indicate the two corner frequencies. (c) The spectral ratio tradeoff between mainshock and aftershock corner frequencies for the optimal coefficient a (see supplement for details on fit modeling). The color version of this figure is available only in the electronic edition.

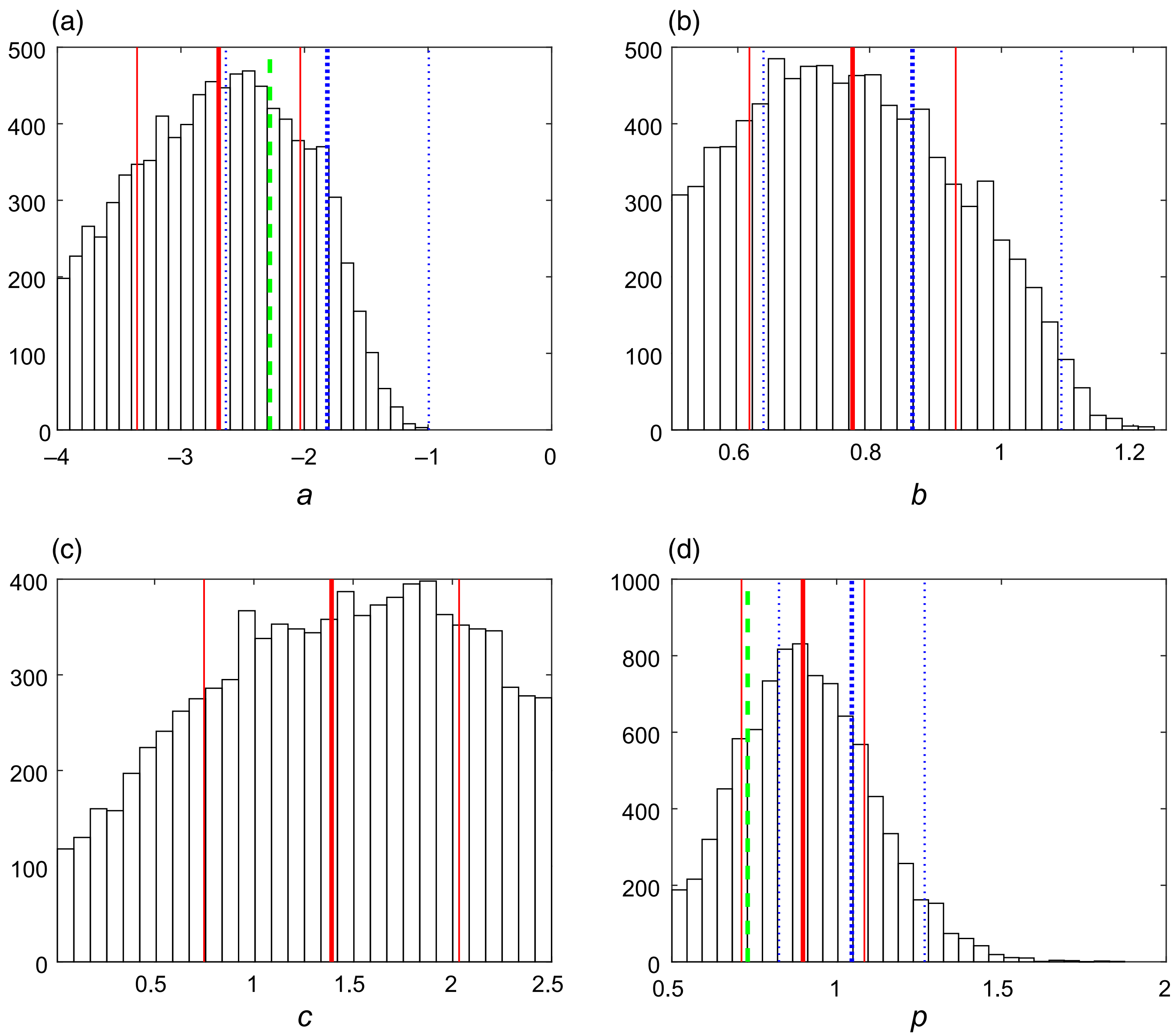

Figure 9. (a–d) Histograms showing the distribution of values for each parameter in the ensemble of model solutions for the Omori decay rate equation. The red solid lines show the mean and standard deviation of the best 10% of ensemble solutions to Bayes modeling for each parameter. The blue-dotted lines show the mean and standard deviation of parameter estimates for stable continental regions (SCRs) by Ebel (2009). The green-dashed lines show the mean estimates for parameters provided by Page *et al.* (2016). The color version of this figure is available only in the electronic edition.

earthquakes with larger minimum magnitudes in their studies of SCR aftershock sequences. Magnitude types were varied in Ebel (2009), and Page *et al.* (2016) used National Earthquake Information Center catalog magnitudes.

Prior work in SCRs has shown the observed catalog value for a median 10-day Båth's law is $\Delta m = 1.9$ (Page *et al.*, 2016), but the authors observe that the median values are larger than the means. In addition, this study only used events within 10 days of the mainshock. This may fail to capture larger aftershocks, artificially making the mainshock–aftershock difference look larger (Page *et al.*, 2016), and in turn making the difference in Delaware more unusual.

Our MCMC inversion results in parameter values $a = -2.694 \pm 0.660$, $b = 0.774 \pm 0.157$, $c = 1.391 \pm 0.642$, $p = 0.898 \pm 0.186$ for the modified Omori decay equation (equation 2). Although some of these values are similar to those found in previous results, others differ significantly.

Our mean a value, indicating overall productivity, does not fall within one standard deviation of the a value given by Ebel (2009) (Table 3). Our mean a value is also lower than that from Page *et al.* (2016). We note, however, that our a value is approximately halfway between the Page *et al.* (2016) SCR value (−2.28) and the stable oceanic regions value of −2.98.

TABLE 3
Aftershock Productivity Parameters

Parameter Set	a	b	c	p
Bayesian MCMC solution	−2.694 ± 0.660	0.774 ± 0.157	1.391 ± 0.642	0.898 ± 0.186
Page *et al.* (2016)	−2.28	–	0.018	0.73
Ebel (2009)	−1.815 ± 0.82	0.865 ± 0.226	0.05	1.046 ± 0.221

Mean and standard deviation ($\pm\sigma$) for the ensemble of model solutions for parameters {a, b, c, p}, compared with results from Page *et al.* (2016) and Ebel (2009). Values for standard deviation for {a, p} were not provided in Page *et al.* (2016). Both reference studies used fixed values for c. Parameter c is in days, other parameters are unitless. MCMC, Markov Chain Monte Carlo; SCR, stable continental region.

TABLE 4
Derived Magnitudes for the Mainshock and Aftershock in Different Scales

Magnitude	Mainshock	Aftershock	Δm
M_L	4.54	**1.75**	2.79
$m_b(Lg)$	4.70	1.84	2.86
M_s	4.04	0.12	3.92
M_w	**4.24**	2.27	1.97

The mainshock magnitude originally used was M_w; the aftershock magnitude used was M_L (listed in bold). Conversion between M_L and $m_b(Lg)$ is from Kim (1998), conversion from $m_b(Lg)$ to M_w is from Rigsby *et al.* (2014), and conversion from $m_b(Lg)$ to M_s is from Lienkaemper (1984). M_L, local magnitude; $m_b(Lg)$, computed short-period Lg magnitude; M_s, computed 20-s surface-wave magnitude; M_w, moment magnitude; Δm, mainshock–aftershock magnitude difference.

The proximity of the continental shelf may play a role in this factor and is an area for further research.

The b value found with Bayesian modeling is consistent with the value $b = 0.863 \pm 0.111$ we found for the maximum-likelihood estimate (Aki, 1965). It is below the global average of ~1 (Frohlich and Davis, 1993), but consistent with values for SCRs (Ebel, 2009) as well as b values for California aftershock sequences observed by Reasenberg and Jones (1989).

The c value, or time offset between the mainshock and the sequence of aftershocks, is the most poorly resolved parameter in the MCMC inversion (Fig. 9, Fig. S6), but also the least relevant for aftershock interpretation. Ebel (2009) uses a fixed value $c = 0.05$ days, which is drawn from Reasenberg and Jones (1989) but not explained. Page *et al.* (2016) used a fixed value $c = 0.018$ days for fitting to SCR aftershocks, in which c was the result of the global fit for all tectonic regimes. We fix the value of $c = 1.526$ days based on $t(\text{main}) - t(\text{first aftershock} \geq M_c)$ for our dataset. This value is larger than in Page *et al.* (2016) and Ebel (2009) because the data we used were from stations deployed after the mainshock, and not from permanent stations that would have been able to record aftershocks that occurred immediately after the mainshock. Inverting for a, b, and p, we obtain similar results of $a = -2.732 \pm 0.662$, $b = 0.790 \pm 0.156$, and $p = 0.920 \pm 0.180$. If instead we fix $c = 0.05$, the MCMC inversion results in $a = -2.896 \pm 0.594$, $b = 0.772 \pm 0.141$, and $p = 0.762 \pm 0.132$. The b value remains stable independent of variations in c value, and changes in a value are within one standard deviation of one another. The p value shows a positive correlation to changes in c (Fig. S6), which is most likely due to the MCMC inversion trying to compensate for the lack of detected aftershocks in the first 1.5 days after the mainshock through a low decay value. Because we know there was at least one aftershock on 1 December 2017 prior to our network deployment (Kim *et al.*, 2018), our results with $c = 1.391$ days account for this time delay.

The value we find for p, or the rate of aftershock sequence decay, is higher than that found by Page *et al.* (2016) but on the low end of the range given by Ebel (2009). This is not surprising, given the limited sample sizes for both prior studies, and we find our value to be generally consistent with both studies.

Despite the observed differences in Båth's law Δm and Omori a values, the subsequent aftershock magnitude distribution followed a typical SCR Gutenberg–Richter distribution. Other related values appear consistent with those reported in previous studies (Ebel, 2009; Page *et al.*, 2016). Our b value, indicating the relative proportion of smaller and larger aftershocks, was consistent with values for SCRs (Ebel, 2009). Similarly, we found a p value for the Omori decay exponent (Utsu, 1961; Reasenberg and Jones, 1989) that is also consistent with prior studies for SCR earthquakes (Ebel, 2009; Page *et al.*, 2016), indicating that the decay in frequency with time of Delaware aftershocks was nominal.

To compare, the 2011 M_w 5.8 Mineral, Virginia, aftershock sequence had a b value of 0.86, a value for the Omori p near 1, and a typical $\Delta m = 1.5$ (Wu *et al.*, 2015; Wu and Chapman, 2017), all consistent with findings for stable continental earthquakes with M ≥ 5. The M_w 4.8 Tewksbury, New Jersey, earthquake in 2024 had a much higher $b = 1.19 \pm 0.03$ and a typical $\Delta m = 1.1$ (Beaucé *et al.*, 2025). Their estimate of the p value ranged from 0.25 to 0.80, corresponding to a slower-than-usual decay; however, the highly heterogeneous local network for detection makes this estimate hard to interpret or compare with other sequences (Beaucé *et al.*, 2025).

Other work has suggested that low-to-moderate-magnitude earthquakes may not be consistent with Båth's parameter for maximum aftershock magnitude (Utsu, 1969; Vere-Jones, 1969; Console *et al.*, 2003). Low aftershock productivity has also been reported for moderate-magnitude earthquakes in South Carolina (Daniels *et al.*, 2019) and Maine (Quiros *et al.*, 2015) (M_w 4.1 and 4.0 respectively) and observed in

Michigan (M_w 4.24) (USGS, n.d.b). Although individually these sequences are not unusual, the occurrence of multiple low productivity sequences among the relatively small pool of M 4+ earthquakes in the CEUS is intriguing. This suggests that aftershock behavior in the intraplate CEUS may not be well modeled by parameters from generic worldwide SCRs and is an avenue for additional research.

In contrast to our work and other previous studies, Dascher-Cousineau *et al.* (2020) evaluated relative productivity for different tectonic settings, source effects, and focal mechanisms; however, their work did not evaluate productivity directly from the Omori *a* value. They argued that an intraplate location could lead to higher-than-average productivity, in contrast to Page *et al.* (2016), but also that this could be mitigated by other factors. In Delaware, these include the primarily strike-slip mechanism of the mainshock and the lithospheric age of the CEUS (Dascher-Cousineau *et al.*, 2020), possibly in combination with the stress drop above the global average (Boyd *et al.*, 2017; Wetzler *et al.*, 2018; Dascher-Cousineau *et al.*, 2020).

Potential causes of Delaware seismicity

One potential contributing factor to seismicity in passive margins is the existence of inherited faults or planes of weakness along which earthquakes might be more likely to occur. Hatcher Jr. *et al.* (2007, Fig. 1) provide a detailed map of the surface geology units in the Salisbury Embayment region. The location of the M_w 4.24 mainshock is approximately at the interface of the Carolina superterrane and the Brunswick (Charleston) terrane in east-central Delaware (Hatcher Jr. *et al.*, 2007). This terrane boundary strikes northeast–southwest at this latitude. It is also the inferred northern end of the Taylorsville rift basin, a Mesozoic rift zone produced by the rifting process that broke up Pangaea in the Triassic–Jurassic (Olsen, 1990; Withjack *et al.*, 1998). The half-graben remaining from the Taylorsville rift has an east-northeast–west-southwest trend (Olsen, 1990; Hatcher Jr. *et al.*, 2007; Withjack *et al.*, 2012). Kim *et al.* (2018) proposed a west-northwest–east-northeast-striking, *S*-dipping fault based on their estimated aftershock alignment and suggested the nodal plane at 103° was the likely fault plane for the mainshock. Although this is not exactly aligned with the orientation of the rift margin, we cannot rule out that rift-related faults were a contributing factor to the generation of the mainshock. However, the northeast–southwest orientation of the terrane boundaries is more oblique to the nodal planes of the mainshock and is therefore less likely to be responsible for this seismicity.

The aftershock locations we find in this article fall along an apparent northwest–southeast striking, southwest-dipping fault (Fig. 6). This plane is oblique to both the nodal planes of the mainshock and the known rift basin structures and terrane boundaries (Withjack *et al.*, 1998; Hatcher Jr. *et al.*, 2007; Kim *et al.*, 2018). There is no known geological structure that strikes parallel to our observed aftershock fault plane. Given that the fault plane evidenced by our aftershocks is otherwise undefined in the local geological maps, it is difficult to constrain what fault properties might be responsible for the low aftershock productivity. However, we can evaluate the combined effect of a northwest–southeast striking, southwest-dipping fault plane with the ambient stress field.

The moment tensor for the mainshock in our study has three consistent solutions: the National Earthquake Information Center, Saint Louis University (USGS, n.d.), and Kim *et al.* (2018). The strikes of the two nodal planes were approximately 0° and 100° for each of these moment tensors (Kim *et al.*, 2018). This would imply a maximum stress direction of ∼55°. Delaware has an overall northeast–southwest (∼45°)-striking stress field, as does the majority of the CEUS (Gardner, 1989; Zoback and Zoback, 1989; Heidbach *et al.*, 2018). This is broadly consistent with the compressive stress inferred from the focal mechanism of the mainshock. Both of these give evidence of a regional stress field characterized by a maximum compressive stress direction oriented northeast–southwest, roughly orthogonal to our observed dipping fault plane. This might suggest that these events are therefore caused by thrusting along the previously unidentified northwest–southeast-striking, southwest-dipping fault. However, given that little is known about this fault, it is difficult to assess the geological contributing factors that might produce our observed low aftershock productivity. It is possible that the mainshock triggered seismicity on a pre-existing, optimally oriented fault zone caused by any one of the earlier repeated episodes of orogenesis and rifting to which the eastern United States has been subjected. The low aftershock productivity may simply reflect the small size of this obliquely oriented fault.

Conclusions

The M_w 4.24 mainshock was the largest earthquake under the ACP in the twenty-first century (ANSS ComCat, Data and Resources). The use of a local network increased the total number of detected aftershocks during the period from late on 1 December to 11 January 2018 by an order of magnitude and lowered the magnitude of completeness for detected events by approximately one magnitude unit, relative to detections with regional stations reported by Kim *et al.* (2018). We observed a lower-than-average aftershock productivity for this sequence, characterized by a high $\Delta m = 2.45$ that is more than twice Båth's law expected difference of $\Delta m = 1.2$ (Richter, 1958; Båth, 1965), and a low *a* value for the Omori decay rate (Reasenberg and Jones, 1989). Our observed *a* value is substantially lower than the mean of other SCR aftershock sequences (Ebel, 2009; Page *et al.*, 2016).

We do not find an unusual stress drop for the Delaware earthquake relative to CEUS events and therefore do not consider stress drop to be a primary factor for the low number of aftershocks. The apparent aftershock fault plane is well aligned for shear failure for thrust faulting (Hardebeck, 2010), but its orientation orthogonal to Mesozoic rift margins may indicate a very small obliquely oriented fault of differing origin. This may be pre-Mesozoic, or may be a splay fault off of the rift bounding faults. The likely small size may contribute toward lower-than-usual aftershock productivity. Our results contribute to our body of knowledge concerning aftershock sequences in SCRs and hold implications for predicting hazards due to aftershock occurrence in intraplate settings.

Data and Resources

Nodal data used in this deployment were gathered on instruments owned by the University of Maryland and is available at: Vedran Lekic and Karen M. Pearson (2017). *Dover, Delaware Aftershock Nodal Deployment* [Data set], International Federation of Digital Seismograph Networks, doi: 10.7914/3gq2-3h19. Broadband data used in this deployment were gathered on instruments owned by the Carnegie Institution for Science and are available at Lara Wagner and Diana Roman (2017). *Delaware 2017 Aftershock Study* [Data set], International Federation of Digital Seismograph Networks, doi: 10.7914/SN/Y3_2017. Regional data used for stress parameter estimation were accessed through the Incorporated Research Institutions for Seismology (now EarthScope) Data Services. These included data from the LD and PE networks: Lamont Doherty Earth Observatory (LDEO), Columbia University (1970). *Lamont–Doherty Cooperative Seismographic Network* [Data set]. International Federation of Digital Seismograph Networks, doi: 10.7914/SN/LD. Penn State University (2004). *Pennsylvania State Seismic Network* [Data set], International Federation of Digital Seismograph Networks, doi: 10.7914/SN/PE. Reference data from the U.S. Geological Survey included: USGS, Earthquake Hazards Program, 2017, Advanced National Seismic System Comprehensive Catalog of Earthquake Events and Products: Various, doi: 10.5066/F7MS3QZH. USGS, Quaternary fault and fold database for the United States available at https://www.usgs.gov/natural-hazards/earthquake-hazards/faults (last accessed February 2021). The supplemental material for this article includes details on the algorithms for location grid search, locations using a 1 km sediment model, stress-drop modeling, magnitude extrapolation for events without locations, and Bayesian Markov Chain Monte Carlo simulation.

Declaration of Competing Interests

The authors acknowledge that there are no conflicts of interest recorded.

Acknowledgments

The authors would like to thank Erin Cunningham, Chao Gao, Steven Golden, Phillip Goodling, Quancheng Huang, Helen Janiszewski, Pete Meehan, Diana Roman, Lisa Schleicher, and Thomas Pratt, who assisted with the installation and retrieval of the temporary deployment of sensors. The authors thank two external reviewers, John Ebel and Andrea Llenos, as well as the Focus Section Guest Editor Oliver Boyd, for insightful comments and feedback that contributed to the article. The authors thank Thomas Pratt for conversations and input to improve the article. The authors thank Nicholas Schmerr for assistance in the archiving of the nodal data. Funding for this work came from the David and Lucille Packard Foundation Fellowship to V. L.

References

Abercrombie, R. E., and A. S. Baltay (2025). Magnitude, depth, and methodological variations of spectral stress drop within the SCEC/USGS community stress drop validation study using the 2019 Ridgecrest earthquake sequence, *Bull. Seismol. Soc. Am.* **115,** no. 6, 2741–2768, doi: 10.1785/0120250056.

Aki, K. (1965). Maximum likelihood estimate of b in the formula log $N = a\text{-}bM$ and its confidence limits, *Bull. Earthq. Res. Inst.* **43,** 237–239.

Allmann, B. P., and P. M. Shearer (2009). Global variations of stress drop for moderate to large earthquakes, *J. Geophys. Res.* **114,** no. 1, 1–22, doi: 10.1029/2008JB005821.

Båth, M. (1965). Lateral inhomogeneities of the upper mantle, *Tectonophysics* **2,** no. 6, 483–514, doi: 10.1016/0040-1951(65)90003-X.

Baxter, S. J. (2000). Catalog of earthquakes in Delaware, *Delaware Geol. Surv. Open File Rept. No. 42*, Delaware Geological Survey, Newark.

Beaucé, E., F. Waldhauser, D. Schaff, W. Y. Kim, and F. Kolawole (2025). The 5 April 2024 M_w 4.8 Tewksbury, New Jersey aftershock sequence resolved with machine-learning-enhanced detection methods, *Geophys. Res. Lett.* **52,** no. 12, doi: 10.1029/2024GL113598.

Boyd, O. S., D. Churchwell, M. P. Moschetti, E. M. Thompson, M. C. Chapman, O. Ilhan, T. L. Pratt, S. K. Ahdi, and S. Rezaeian (2024). Sediment thickness map of United States Atlantic and Gulf Coastal Plain strata, and their influence on earthquake ground motions, *Earthq. Spectra* **40,** no. 1, 89–112, doi: 10.1177/87552930231204880.

Boyd, O. S., D. E. McNamara, S. Hartzell, and G. Choy (2017). Influence of lithostatic stress on earthquake stress drops in North America, *Bull. Seismol. Soc. Am.* **107,** no. 2, 856–868, doi: 10.1785/0120160219.

Brune, J. N. (1970). Tectonic stress and the spectra of seismic shear waves from earthquakes, *J. Geophys. Res.* **75,** no. 26, 4997–5009, doi: 10.1029/JB075i026p04997.

Calais, E., T. Camelbeeck, S. Stein, M. Liu, and T. J. Craig (2016). A new paradigm for large earthquakes in stable continental plate interiors, *Geophys. Res. Lett.* **43,** no. 20, 10,621–10,637, doi: 10.1002/2016GL070815.

Hatcher, R. D., Jr., M. P. Carlson, J. H. McBride, and J. R. M. Catalán (2007). Geologic terranes of the south-eastern U. S., in *4-D Framework of Continental Crust*, R. D. Hatcher, M. P. Carlson, J. H. McBride, and J. R. M. Catalán (Editors), Geological Society of America, doi: 10.1130/MEM200.

Chen, K.-C., J.-M. Chiu, and Y.-T. Yang (1996). Shear-wave velocity of the sedimentary basin in the upper Mississippi embayment using S-to-P converted waves, *Bull. Seismol. Soc. Am.* **86,** no. 3, 848–856.

Chung, D. H., and D. L. Bernreuter (1981). Regional relationships among earthquake magnitude scales, *Rev. Geophys.* **19,** no. 4, 649–663, doi: 10.1029/RG019i004p00649.

Console, R., A. M. Lombardi, M. Murru, and D. Rhoades (2003). Båth's law and the self-similarity of earthquakes, *J. Geophys. Res.* **108,** no. B2, doi: 10.1029/2001jb001651.

Cunningham, E., and V. Lekic (2020). Constraining properties of sedimentary strata using receiver functions: An example from the

Atlantic Coastal Plain of the southeastern United States, *Bull. Seismol. Soc. Am.* **110,** no. 2, 519–533, doi: 10.1785/0120190191.

Daniels, C., Z. Peng, Q. Wu, S. Ni, X. Meng, D. Yao, L. S. Wagner, and K. M. Fischer (2019). The 15 February 2014 M_w 4.1 South Carolina earthquake sequence: Aftershock productivity, hypocentral depths, and stress drops, *Seismol. Res. Lett.* **91,** no. 1, 452–464, doi: 10.1785/0220190034.

Dascher-Cousineau, K., E. E. Brodsky, T. Lay, and T. H. W. Goebel (2020). What controls variations in aftershock productivity? *J. Geophys. Res.* **125,** no. 2, doi: 10.1029/2019JB018111.

Ebel, J. E. (2009). Analysis of aftershock and foreshock activity in stable continental regions: Implications for aftershock forecasting and the hazard of strong earthquakes, *Seismol. Res. Lett.* **80,** no. 6, 1062–1068, doi: 10.1785/gssrl.80.6.1062.

Ellsworth, W. L., K. Imanishi, J. H. Luetgert, J. Kruger, and J. Hamilton (2011). The M_w 5.8 Virginia earthquake of August 23, 2011 and its aftershocks: A shallow high stress drop event, *AGU Fall Meeting Abstracts*, p. S14B-05.

Frohlich, C., and S. D. Davis (1993). Teleseismic *b* values; Or, Much ado about 1.0, *J. Geophys. Res.* **98,** no. B1, 631–644.

Gardner, T. W. (1989). Neotectonism along the Atlantic passive continental margin: A review, *Geomorphology* **2,** nos. 1/3, 71–97, doi: 10.1016/0169-555X(89)90007-X.

Gibbons, S. J., and F. Ringdal (2006). The detection of low magnitude seismic events using array-based waveform correlation, *Geophys. J. Int.* **165,** no. 1, 149–166, doi: 10.1111/j.1365-246X.2006.02865.x.

Hansen, H. J. (1988). Buried rift basin underlying coastal plain sediments, central Delmarva Peninsula, Maryland, *Geology* **16,** no. 9, 779–782.

Hardebeck, J. (2010). Aftershocks are well aligned with the background stress field, contradicting the hypothesis of highly heterogeneous crustal stress, *J. Geophys. Res.* **115,** no. 12, doi: 10.1029/2010JB007586.

Hartzell, S., C. Mendoza, and Y. Zeng (2013). Rupture model of the 2011 Mineral, Virginia, earthquake from teleseismic and regional waveforms, *Geophys. Res. Lett.* **40,** no. 21, 5665–5670, doi: 10.1002/2013GL057880.

Heidbach, O., M. Rajabi, X. Cui, K. Fuchs, B. Müller, J. Reinecker, K. Reiter, M. Tingay, F. Wenzel, F. Xie, *et al.* (2018). The World Stress Map database release 2016: Crustal stress pattern across scales, *Tectonophysics* **744,** 484–498, doi: 10.1016/j.tecto.2018.07.007.

Herrmann, R. B. (1979). Surface wave focal mechanisms for eastern North American earthquakes with tectonic implications, *J. Geophys. Res.* **84,** no. 8, 3543–3552, doi: 10.1029/JB084iB07p03543.

Kaneko, Y., and P. M. Shearer (2014). Seismic source spectra and estimated stress drop derived from cohesive-zone models of circular subshear rupture, *Geophys. J. Int.* **197,** no. 2, 1002–1015, doi: 10.1093/gji/ggu030.

Kim, W. (1998). The ML scale in eastern North America, *Bull. Seismol. Soc. Am.* **88,** no. 4, 935–951.

Kim, W. Y., M. Gold, J. Ramsay, A. Meltzer, D. Wunsch, S. Baxter, V. Lekic, P. Goodling, K. Pearson, L. Wagner, *et al.* (2018). The M_w 4.2 Delaware earthquake of 30 November 2017, *Seismol. Res. Lett.* **89,** no. 6, 2447–2460, doi: 10.1785/0220180124.

LeTourneau, P. M. (2003). Stratigraphic architecture and paleomagnetic reversal stratigraphy of the Late Triassic Taylorsville basin, Virginia and Maryland, in *The Great Rift Valleys of Pangea in Eastern North America*, LeTourneau, P. M., and P. E. Olsen (Editors), Vol. 2, Columbia University Press, New York, 12–58.

Lienkaemper, J. J. (1984). Comparison of two surface-wave magnitude scales: M of Gutenberg and Richter (1954) and Ms of "Preliminary Determination of Epicenters," *Bull. Seismol. Soc. Am.* **74,** no. 6, 2357–2378.

Madariaga, R. (1976). Dynamics of an expanding circular fault, *Bull. Seismol. Soc. Am.* **66,** no. 3, 639–666, doi: 10.1086/622062.

Miller, K. G., J. V. Browning, P. J. Sugarman, D. H. Monteverde, D. C. Andreasen, C. Lombardi, J. Thornburg, Y. Fan, and R. E. Kopp (2017). Lower to mid-Cretaceous sequence stratigraphy and characterization of CO2 storage potential in the Mid-Atlantic U.S. Coastal Plain, *J. Sedimentary Res.* **87,** no. 6, 609–629, doi: 10.2110/jsr.2017.33.

Nuttli, O. W. (1973). Seismic wave attenuation and magnitude relations for eastern North America, *J. Geophys. Res.* **78,** no. 5, 876–885, doi: 10.1029/jb078i005p00876.

Olsen, P. E. (1990). Tectonic, climatic, and biotic modulation of Lacustrine ecosystems—Examples from Newark supergroup of eastern North America, in *Lacustrine Basin Exploration: Case Studies and Modern Analogs*, B. Katz (Editor), American Association of Petroleum Geologists, 209–224.

Olsson, R. K., T. G. Gibson, H. J. Hansen, and J. P. Owens (1988). Geology of the northern Atlantic coastal plain: Long Island to Virginia, in *The Atlantic Continental Margin: U.S.*, R. E. Sheridan and J. A. Grow (Editors), The Geological Society of America, Boulder, Colorado, 87–105.

Omori, F. (1895). On the aftershocks of earthquakes, *J. Coll. Sci. Imp. Univ. Jpn.* **7,** no. 2, 111–200.

Page, M. T., N. van Der Elst, J. Hardebeck, K. Felzer, and A. J. Michael (2016). Three ingredients for improved global aftershock forecasts: Tectonic region, time-dependent catalog incompleteness, and intersequence variability, *Bull. Seismol. Soc. Am.* **106,** no. 5, 2290–2301, doi: 10.1785/0120160073.

Pope, J. P., D. C. Andreasen, E. R. Mcfarland, and M. K. Watt (2016). Digital elevations and extents of regional hydrogeologic units in the Northern Atlantic Coastal Plain aquifer system from Long Island, New York, to North Carolina, *U.S. Geol. Surv.*, Reston, Virginia, doi: 10.3133/ds996.

Pratt, T. L. (2018). Characterizing and imaging sedimentary strata using depth-converted spectral ratios: An example from the Atlantic Coastal Plain of the eastern United States, *Bull. Seismol. Soc. Am.* **108,** no. 5A, 2801–2815, doi: 10.1785/0120180046.

Quiros, D. A., A. Cabolova, L. D. Brown, C. Chen, J. E. Ebel, and J. Starr (2015). Aftershock imaging with dense arrays (AIDA) following the M_w 4.0 Waterboro earthquake of 16 October 2012 Maine, U.S.A., *Seismol. Res. Lett.* **86,** no. 3, 1032–1039, doi: 10.1785/0220140169.

Reasenberg, P. A., and L. M. Jones (1989). Earthquake hazard after a mainshock in California, *Science* **243,** no. 4895, 1173–1176, doi: 10.1126/science.243.4895.1173.

Richter, C. F. (1958). *Elementary Seismology*, W.H. Freeman, San Francisco, doi: 10.5408/0022-1368-7.1.21.

Rigsby, C., R. B. Herrmann, and H. Benz (2014). An investigation of *MbLg* versus M_w for eastern North America, *Seismol. Res. Lett.* **85,** no. 3, 625–630.

Saikia, C. K. (1994). Modified frequency-wavenumber algorithm for regional seismograms using Filon's quadrature: Modelling *Lg* waves in eastern North America, *Geophys. J. Int.* **118,** 142–158.

Sbar, M. L., R. R. Jordan, C. D. Stephens, T. E. Pickett, K. D. Woodruff, and C. G. Sammis (1975). The Delaware-New Jersey earthquake of February 28, 1973, *Bull. Seismol. Soc. Am.* **65,** no. 1, 85–92.

Schaff, D. P., and F. Waldhauser (2010). One magnitude unit reduction in detection threshold by cross correlation applied to Parkfield (California) and China seismicity, *Bull. Seismol. Soc. Am.* **100,** no. 6, 3224–3238, doi: 10.1785/0120100042.

Shi, Y., and B. A. Bolt (1982). The standard error of the magnitude-frequency *b* value, *Bull. Seismol. Soc. Am.* **72,** no. 5, 1677–1687.

Slinkard, M., D. Schaff, N. Mikhailova, S. Heck, C. Young, and P. G. Richards (2014). Multistation validation of waveform correlation techniques as applied to broad regional monitoring, *Bull. Seismol. Soc. Am.* **104,** no. 6, 2768–2781, doi: 10.1785/0120140140.

Soto-Cordero, L., A. Meltzer, and J. C. Stachnik (2018). Crustal structure, intraplate seismicity, and seismic hazard in the mid-Atlantic United States, *Seismol. Res. Lett.* **89,** no. 1, 241–252, doi: 10.1785/0220170084.

Spoljaric, N. (1973). Normal faults in basement rocks of the northern coastal plain, Delaware, *Bull. Geol. Soc. Am.* **84,** no. 8, 2781–2784.

Stein, S., and M. Liu (2009). Long aftershock sequences within continents and implications for earthquake hazard assessment, *Nature* **462,** no. 7269, 87–89, doi: 10.1038/nature08502.

Stover, C. W., and J. L. Coffman (1993). *Seismicity of the United States, 1568-1989*, United States Government Printing Office, Denver.

Toda, S., and R. S. Stein (2018). Why aftershock duration matters for probabilistic seismic hazard assessment, *Bull. Seismol. Soc. Am.* **108,** no. 3, 1414–1426, doi: 10.1785/0120170270.

U.S. Geological Survey (USGS) (n.d.a). Event page M 4.1–3 km NNE of Little Creek, Delaware, available at https://earthquake.usgs.gov/earthquakes/eventpage/us1000bjkn/executive#executive (last accessed December 2025).

USGS (n.d.b). Event page M 4.2–5 km S of Galesburg, Michigan, available at https://earthquake.usgs.gov/earthquakes/eventpage/us20002avh/executive (last accessed October 2025).

Utsu, T. (1961). A statistical study on the occurrence of aftershocks, *Geophysics* **30,** 521–605.

Utsu, T. (1969). Aftershocks and earthquake statistics: Some parameters which characterize an aftershock sequence and their interrelations, *J. Faculty Sci. Hokkaido Univ.* **3,** no. 3, 129–195.

Vere-Jones, D. (1969). A note on the statistical interpretation of Bath's law, *Bull. Seismol. Soc. Am.* **59,** no. 4, 1535–1541.

Wetzler, N., T. Lay, E. E. Brodsky, and H. Kanamori (2018). Systematic deficiency of aftershocks in areas of high coseismic slip for large subduction zone earthquakes, *Sci. Adv.* **4,** no. 2, 1–10, doi: 10.1126/sciadv.aao3225.

Withjack, M. O., R. W. Schlische, M. L. Malinconico, and P. E. Olsen (2012). *Rift-Basin Development: Lessons from the Triassic-Jurassic Newark Basin of Eastern North America*, Geological Society of Special Publication, Vol. 369, 301–321, doi: 10.1144/SP369.13.

Withjack, M. O., R. W. Schlische, and P. E. Olsen (1998). Diachronous rifting, drifting, and inversion on the passive margin of central eastern North America: An analog for other passive margins, *Am. Assoc. Pet. Geol. Bull.* **82,** no. 5A, 817–835.

Wu, Q., and M. C. Chapman (2017). Stress-drop estimates and source scaling of the 2011 Mineral, Virginia, mainshock and aftershocks, *Bull. Seismol. Soc. Am.* **107,** no. 6, 2703–2720, doi: 10.1785/0120170098.

Wu, Q., M. C. Chapman, and J. N. Beale (2015). The aftershock sequence of the 2011 Mineral, Virginia, earthquake: Temporal and spatial distribution, focal mechanisms, regional stress, and the role of Coulomb stress transfer, *Bull. Seismol. Soc. Am.* **105,** no. 5, 2521–2537, doi: 10.1785/0120150032.

Yoon, C. E., O. O'Reilly, K. J. Bergen, and G. C. Beroza (2015). Earthquake detection through computationally efficient similarity search, *Sci. Adv.* **1,** 1–13, doi: 10.1126/sciadv.1501057.

Zoback, M. L., and M. D. Zoback (1989). Tectonic stress field of the continental United States, in *Geophysical framework of the continental United States*, L. C. Pakiser and W. D. Mooney (Editors), Geological Society of America, Boulder, Colorado, 523–539, doi: 10.1130/MEM172-p523.

Manuscript received 18 September 2025
Published online 4 February 2026